Environmental drivers constraining the seasonal variability of satellite-observed methane at Northern high latitudes

Ella Kivimäki[1], Tuula Aalto[2], Michael Buchwitz[3], Kari Luojus[1], Jouni Pulliainen[1], Kimmo Rautiainen[1], Oliver Schneising[3], Anu-Maija Sundström[1], Johanna Tamminen[1], Aki Tsuruta[2], and Hannakaisa Lindqvist[4]

[1]Space and Earth Observation Centre, Finnish Meteorological Institute, Helsinki, Finland
[2]Climate Research, Finnish Meteorological Institute, Helsinki, Finland
[3]Institute of Environmental Physics (IUP), University of Bremen, Bremen, Germany
[4]Space and Earth Observation Centre, Finnish Meteorological Institute, Sodankylä, Finland

Correspondence: E. Kivimäki (ella.kivimaki@fmi.fi)

Abstract. Methane emissions from Northern high-latitude wetlands are associated with large uncertainties, especially in the rapidly warming climate. Satellite observations of column-averaged methane concentrations (XCH_4) in the atmosphere exhibit variability due to time-varying sources and sinks. In this study, we investigate how environmental variables, such as temperature, soil moisture, snow cover, and the hydroxyl radical (OH) sink of methane, explain the seasonal variability of column-averaged methane concentrations (XCH_4) observed from space over Northern high-latitude wetland areas. We use XCH_4 data obtained from the TROPOMI instrument aboard the Sentinel-5 Precursor satellite, retrieved using the Weighting Function Modified Differential Optical Absorption Spectroscopy (WFMD) algorithm. Environmental variables are derived primarily from meteorological reanalysis datasets, with satellite-based data used for snow cover and soil freeze-thaw dynamics, and modeled data for the OH sink. Our analysis focuses on five case study regions, including two in Finland and three in Russian Siberia, covering the period from 2018 to 2023. Our findings reveal that environmental variables have a systematic impact on XCH_4 variability: the seasonal variability is most strongly influenced by snow cover and soil water volume, while daily variability is primarily affected by soil temperature. Our results are largely consistent with in-situ-based local studies but the role of snow is more pronounced. Our results demonstrate how satellite XCH_4 observations can be used to study the seasonal variability of atmospheric methane over large wetland regions. The results imply that satellite observations of atmospheric composition, along with other Earth Observations as well as meteorological reanalysis data can be jointly informative of the processes controlling the emissions in Northern high latitudes.

1 Introduction

Methane (CH_4) is the second most important anthropogenic greenhouse gas (GHG), in terms of its total radiative forcing, following carbon dioxide (CO_2). In recent decades, methane concentrations in the atmosphere have experienced a rapid growth rate, the drivers of which are being debated (e.g.Turner et al. 2017; Skeie et al. 2023). Globally, approximately 65% of methane emissions are anthropogenic, with agriculture and waste management being the primary contributors (Saunois et al., 2024;

Jackson et al., 2024). The main natural source is wetlands and inland freshwater systems. The main sink of methane is chemical loss by hydroxyl radicals (OH), primarily in the troposphere. According to Saunois et al. (2020, 2024) 65% of the global emissions originate from south of 30°N, and methane emissions from high latitudes (north of 60°N) represent only 4% of

25 the global total. However, uncertainties in the high-latitude regions are notably larger, with atmospheric measurement-based top-down estimates having uncertainties exceeding ±20%, compared to less than ±5% globally. Since 1979, the high Northern latitudes have been warming nearly four times faster than the global average (Rantanen et al., 2022), a phenomenon with potentially significant consequences for methane emissions in these sensitive areas: for example, a warming climate can lead to an extended growing season or longer shoulder seasons, during which emissions are higher on a monthly basis, compared to

30 colder months (Zona et al., 2015; Bao et al., 2021; Rößger et al., 2022). Additionally, warming can directly increase methane emissions from specific land cover types (Rehder et al., 2023), or thaw permafrost, potentially leading to rising emissions: continuous permafrost regions, for instance, have shown lower emissions compared to discontinuous permafrost regions (Erkkilä et al., 2023; Rößger et al., 2022).

Seasonal variability in methane concentration in the Northern Hemisphere is driven by the seasonality of its sinks and

35 sources, while in the Southern Hemisphere, the sink dominates (East et al., 2024). Although anthropogenic methane emissions show some seasonal variability in the high latitudes (Tsuruta et al., 2023), likely related to factors such as gas production or biomass burning (Berchet et al., 2015), natural emissions show much stronger seasonal variability, mainly driven by wetland emissions (East et al., 2024; Tsuruta et al., 2023). Methane emissions from wetlands are influenced by wetland conditions and environmental variables, including, for example, temperature (Howard et al., 2020; Rinne et al., 2018; Kittler et al., 2017),

40 soil moisture and water table level (Virkkala et al., 2024), and snow cover together with soil frost (Rößger et al., 2022; Zona et al., 2015; Mastepanov et al., 2013; Rinne et al., 2007). The methane emissions from wetlands are primarily driven by anaerobic processes, where methanogens produce methane by reducing carbon dioxide with hydrogen or breaking down acetate (Bridgham et al., 2013). Such processes are sensitive to environmental conditions that can limit microbial activity, particularly through changes in water availability. Both overly dry and overly wet soils can reduce microbial activity, as suitable moisture

45 levels are required for microbial decomposition. Freezing of the soil, in particular, can limit the availability of liquid water, slowing microbial processes. Furthermore, the main sink of methane, oxidation by OH radicals, has a strong seasonality driven by the number of OH radicals, which is influenced by seasonal variations in their production: OH is primarily produced by the photolysis of ozone in the presence of water vapor, and its concentration fluctuates with factors such as temperature, humidity, and UV radiation (Zhao et al., 2019; Travis et al., 2020). These meteorological factors vary seasonally especially in the mid-

50 dle and high latitudes, leading to seasonal variation of the OH sink. Additionally, when considering methane concentrations throughout the atmosphere, transport must be accounted for due to methane's lifetime of approximately nine years (Saunois et al., 2024). Transport patterns can affect the seasonal variability of methane over long time scales, and changes in transport patterns and emissions in other regions might influence observed concentrations elsewhere (Dowd et al., 2023).

Methane concentrations have often been studied using in situ measurements and models. In situ measurements can accurately

55 measure the methane concentration or flux at a single point close to the ground or in a tower. Their advantage lies in their high accuracy and continuous time series, allowing the use of a network of stations for precise calculations of the regional or global

methane budget. However, gaps in the measurement network hamper the precise localization of emissions and the results are difficult to extrapolate to larger areas. This is because in situ measurements often represent specific conditions, such as particular land cover, vegetation type, soil humidity, and local climate. Additionally, these measurements require electricity
60 and access to the measurement site and, therefore, the flux measurements are often limited to the thaw and snow-free seasons due to maintenance reasons. Models, on the other hand, can describe large-scale phenomena, but they require comprehensive observations to model processes accurately.

The use of satellites in GHG studies has been possible since the 2000s. Satellite observations of methane concentrations in the near-infrared wavelengths started in 2002, when SCIAMACHY onboard Envisat was launched (Buchwitz et al., 2005).
65 The Greenhouse Gases Observing Satellite (GOSAT), launched in 2009, was the first satellite dedicated to GHG observations (Kuze et al., 2009), followed by the TROPOspheric Monitoring Instrument (TROPOMI) onboard the Copernicus Sentinel-5 Precursor satellite in 2017. In addition to these missions, small satellites such as GHGSat also measure methane concentrations, but their utility for large-scale analysis is limited due to their narrow swath and infrequent revisit times. From SCIAMACHY to TROPOMI, both spatial and temporal resolutions have significantly improved; for example, pixel sizes have decreased from
70 tens of kilometres to a few kilometres, and revisit times have reduced from several days to one day.

Satellites observe column-averaged dry-air mole fraction of methane (XCH_4), which is retrieved from solar radiation in the near-infrared wavelengths reflected by the atmosphere or ground surface. Therefore, satellite observations of methane are dependent on sunlight. At high latitudes, the lack of sunlight causes a so-called winter gap in GHG satellite observations, as measurements cannot be conducted due to the sun being close to or beyond the horizon. In addition to large solar zenith angles,
75 cloud cover presents challenges for retrieval algorithms. Additionally, surfaces with a spectrally dependent reflectance, such as snow cover (Mikkonen et al., 2024), can introduce retrieval errors (Lorente et al., 2022). Despite these factors that limit data availability in the Northern high latitudes, updated and improved retrieval algorithms and the high spatial coverage of TROPOMI have reduced the length of the winter data gap at high latitudes. For the latest version of Weighting Function Modified Differential Optical Absorption Spectroscopy retrievals (WFMD v1.8; Schneising et al. 2019, 2023), the observational
80 coverage is, in principle, gapless when considering areas above 50°N overall (Lindqvist et al., 2024). Satellite observations of methane have been used in a wide range of studies, for example, to identify the location and intensity of local point sources (Vanselow et al., 2024; Barré et al., 2021), as well as to investigate variations in methane trends (Hachmeister et al., 2024; Kivimäki et al., 2019). Additionally, methane satellite retrievals have been widely utilized to inform inversion models on methane concentrations (Tsuruta et al., 2023; Liang et al., 2023; Pandey et al., 2016).

85 In this study, we investigate how environmental variables explain the seasonal variability of satellite-observed column-averaged methane concentrations over high-latitude wetland areas. Our aim is to determine how environmental variables, related to methane emissions, together with methane loss by OH, influence total-column concentrations. Based on the in situ measurement findings presented above, we focus particularly on the roles of temperature, soil moisture, snow cover, soil freeze and thaw, and the impact of the OH sink, while also examining whether our results align with these in situ findings.
90 We concentrate on high-latitude wetland areas because, as shown by East et al. (2024), ensemble forward model runs are not always able to accurately reproduce the seasonal methane cycle in the Northern Hemisphere due to incomplete wetland

emission inventories. Satellite observations of methane would be valuable in complementing inversion results, as they could provide new insights that help reduce uncertainties in the global methane budget and ultimately improve our understanding of the increasing and varying methane trend. In Section 2, we introduce the datasets used, followed by the methods in Sect. 3.

95   Section 4 presents and discussed the results and the conclusions are presented in Sect. 5.

2   Data sets

2.1   TROPOMI WFMD XCH$_4$ product

The TROPOspheric Monitoring Instrument (TROPOMI) on board the Copernicus Sentinel-5 Precursor (S5P) satellite was launched in October 2017 and it is dedicated to produce observations for air quality and climate monitoring. With its wide

100   swath of approximately 2600 km, a daily global coverage can be attained. Currently, two retrieval algorithms are generated to retrieve the column-averaged dry-air mole fraction of methane (XCH$_4$) from the near-infrared spectra: the operational TROPOMI XCH$_4$ product, developed by the SRON Netherlands Institute for Space Research (Hu et al., 2018; Lorente et al., 2021), and the Weighting Function Modified Differential Optical Absorption Spectroscopy (WFMD) algorithm, developed by the University of Bremen (Schneising et al., 2019, 2023). In this study, we use XCH$_4$ concentrations retrieved by the WFMD

105   algorithm due to its accuracy and suitability for our analysis. The WFMD v1.8 product shows no seasonal bias when comparing to high-latitude ground-based observations and AirCore data, resulting in lower mean bias and standard deviation (Lindqvist et al., 2024). Furthermore, the WFMD product provides significantly more data from high Northern latitudes, particularly during the spring months, and features a shorter winter gap.

   The WFMD algorithm retrieves simultaneously the column-averaged dry-air mole fractions of CH$_4$ and carbon monoxide

110   (CO). The WFMD algorithm employs a linear least-squares retrieval which uses scaling or shifting of pre-selected atmospheric vertical profiles. The linearised radiative transfer model is fitted to the measured sun-normalised radiance to obtain the vertical columns of CH$_4$ and CO. The retrieval uses look-up tables for fast solutions and accounts for a range of typical atmospheric conditions, e.g. different solar zenith angles, surface albedos, and temperatures. The latest version of WFMD, version 1.8, includes significant changes compared to the previous version aimed at improving retrieval performance for different spec-

115   tral albedos and updating the digital elevation model to reduce bias associated with topography, especially at high latitudes (Schneising et al., 2023; Hachmeister et al., 2022). In addition, the quality filter was refined in the post-processing, which improved cloud filtering over the Arctic. The improvement was particularly pronounced for water areas in the Arctic, but the precision of the cloud-free classification for land observations also increased significantly. At the time of writing of this paper, WFMD v1.8 is the latest available retrieval version.

120   ### 2.2   IMS Daily Northern Hemisphere Snow and Ice Analysis product

Interactive Multisensor Snow and Ice Mapping System (IMS) snow cover and sea ice analysis products from the U.S. National Ice Center (USNIC) are derived from a variety of different data sources, including satellite images and in situ observations.

The daily data set is available since February 1997 and it is produced in three different spatial resolutions: 1 km, 4 km, and 24 km. The data have a four-class classification method for a surface refarding snow and ice: open water, land without snow, sea
125 or lake ice, and snow-covered land.

In our analysis, we used only data over land, i.e. land without snow and snow-covered land classes. We used the 24 km resolution data version for the time period from 2018 to 2023 (U.S. National Ice Center., 2008).

2.3   The Copernicus Global Land Monitoring Service Snow Water Equivalent product

The Copernicus Global Land Service Snow Water Equivalent (SWE) product provides daily estimates of the equivalent amount
130 of liquid water stored in the snowpack across the Northern Hemisphere, with a spatial resolution of 5 km (Takala et al., 2011; Luojus et al., 2021). Snow presence is identified using optical satellite observations, while SWE values are derived through assimilation of passive microwave satellite data and snow depth measurements. Areas covered by lakes, sea ice, mountains, glaciers, and permanent ice are excluded from the dataset. The daily dataset is available since January 2006 and is updated in near real-time.

135 To describe the amount of snow in our case study regions we used SWE data from 2018 to 2023.

2.4   SMOS Level 3 Soil Freeze and Thaw product

The European Space Agency's (ESA) Soil Moisture and Ocean Salinity (SMOS) Soil Freeze and Thaw (F/T) product provides an operational satellite-derived, Level 3 soil freeze and thaw state dataset across the Northern Hemisphere (Rautiainen et al., 2016; ESA, 2023). The observations from the SMOS satellite, primarily designed to measure soil moisture over land and
140 surface salinity over oceans, are the basis for the F/T product. This dataset is generated by the Finnish Meteorological Institute using SMOS Level 3 gridded brightness temperature data provided by the Centre Aval de Traitement des Données SMOS (CATDS) (CATDS, 2022; Al Bitar et al., 2017).

The processing algorithm for the SMOS F/T product integrates two auxiliary datasets, 2-meter air temperature and snow cover data, to refine the accuracy of the freeze-thaw classifications and mitigate obvious misclassifications. The soil state is
145 categorized into three levels: frozen, partially frozen, and thawed soil.

The product covers the time period from 2010 to the present, with daily operational updates available at a latency of approximately one day, ensuring its relevance for ongoing research and applications. The data resolution is 25 km × 25 km, structured on the Equal-Area Scalable Earth (EASE2) grid. For this study, we utilized SMOS v3 data for the years 2019–2023, focusing on ascending orbit data, as these are less affected by radio frequency interference (RFI) over the Eurasian continent Oliva et al.
150 (2016) compared to the descending orbits. Since late 2022, the war in Ukraine has significantly increased RFI, particularly over Europe, leading to a substantial reduction in usable data in 2023. This has affected the analysis and results presented in this paper.

2.5 ERA5 reanalysis data

The European Centre for Medium-Range Weather Forecasts (ECMWF) produces the ERA5 reanalysis, which is widely used as a global meteorologica dataset for scientific purposes (Hersbach et al., 2020). ERA5 provides large data sets of variables related to atmosphere, ocean-waves and land-surface quantities. Reanalysis is a scientific method where the global past observations are integrated into a current advanced computer models, allowing the reconstruction of past atmospheric or land conditions globally, even over areas without in situ observations. ERA5 is based on Integrated Forecasting System (IFS) and is therefore primarily an atmospheric model, but it is coupled with a land surface model and a wave model to estimate land and ocean parameters. ERA5 Land (Muñoz Sabater et al., 2021) variables are generated using advanced data assimilation techniques that integrate various observations to provide accurate and high-resolution land surface data. The horizontal resolution of ERA5 is 31 km and there are 137 vertical layers and the current hourly data on single levels cover time the period from 1940 to present. For the public reanalysis product, the data have been regridded for 0.25° x 0.25° regular grid. ERA5 is widely used for meteorological research and has been developed since 1950.

For this study, we used hourly data on single levels from 2018 to 2023 (Hersbach et al., 2018). The obtained variables were 2m temperature, soil temperature and volumetric soil water at Layer 1. Layer 1 represents the soil depth between 0–7 cm, where the surface is located at 0 cm. In the model, the 2m temperature is calculated by interpolating between the lowest model level and the Earth's surface. Soil temperature represents the temperature at the middle of the layer, calculated by estimating heat transfer between the layers. The soil water volume takes into account soil texture and classification, soil depth, and the underlying groundwater level (ECMWF, 2018).

2.6 CH_4 loss by OH radicals

The tropospheric OH concentrations were estimated based on Spivakovsky et al. (2000), but scaled by 0.92 globally following the optimized estimates using methyl chloroform data (Huijnen et al., 2010; Houweling et al., 2014). The stratospheric OH loss was calculated based on Brühl and Crutzen (1993). The CH_4 loss based on the OH fields was calculated using the global Eulerian atmospheric chemistry transport model TM5 (Krol et al., 2005). TM5 was run at the resolution of 6° x 4° (latitude x longitude) x 25 vertical levels globally constrained by 3-hourly interpolated ECMWF ERA5 meteorological fields, and using posterior CH_4 fluxes from CTE-CH_4 (Tsuruta et al., 2017; Saunois et al., 2024). The chemical reactions were calculated offline, such that the prescribed OH fields and reaction rates were used in the simulation. The monthly total OH losses were calculated for the entire latitude zone 57°N–70°N.

3 Methods

The methods used to define the case study areas, process the data sets, and study the links between the environmental variables and the variability of XCH$_4$ are described as follows. First, the case study areas were defined based on wetland data. Next, the gap filling process and the fitting of the seasonal cycle to the XCH$_4$ time series are explained. The methods for gridding
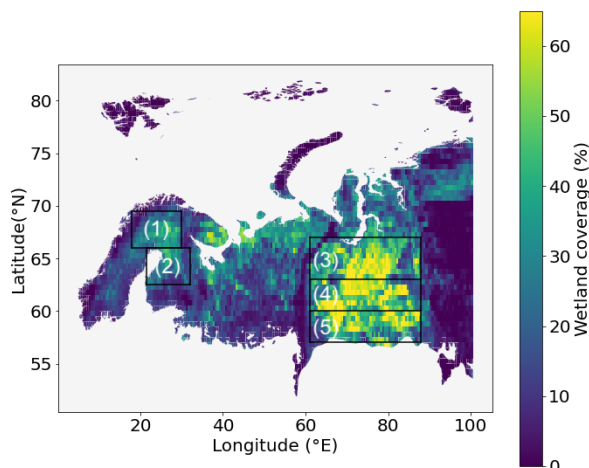
Figure 1. Northern Finland (1), Southern Finland (2), Northern Siberia (3), Middle Siberia (4) and Southern Siberia (5) case study areas marked over BAWLD total wetland coverage map.

Table 1. Total wetland fraction and three most significant wetland types in the five case study regions based on BAWLD wetland data (Olefeldt et al., 2021). In some of the regions, there are also other wetland types. Therefore, the total fraction does not necessarily match the sum of the three types listed here.

	Total wetland (%)	Bog (%)	Permafrost bog (%)	Fen(%)
Northern Finland 66–69.5°N, 18–30°E	26.5	11.2	0.4	13.8
Southern Finland 62.5–66°N, 21.5–32°E	23.3	12.6	0.0	10.0
Northern Siberia 63–67°N, 61–88°E	40.2	5.5	19.1	8.8
Middle Siberia 60–63°N, 61–88°E	45.8	20.8	1.2	19.7
Southern Siberia 57–60°N, 61–88°E	40.8	21.0	0.0	16.9

and averaging environmental variables to align them with the XCH_4 time series are then outlined. Finally, the application of

185   random forest feature importance and permutation importance to study the connections between the time series are described.
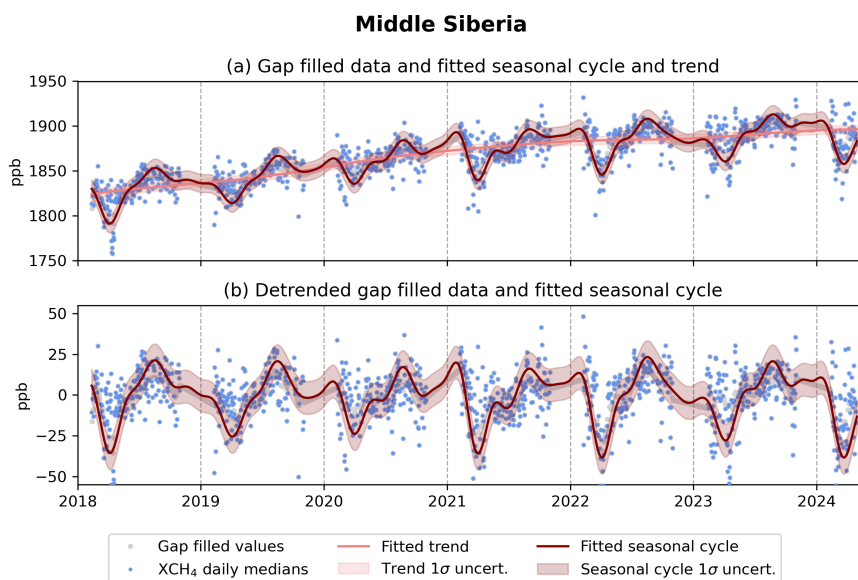
Figure 2. (a) TROPOMI WFMD daily median XCH$_4$ (blue dots), gap-filled XCH$_4$ values (grey dots) and fitted seasonal cycle and trend, and their uncertainties (red and shaded red) for Middle Siberia. (b) shows the same for the detrended time series.

3.1 Defining the case study areas

To investigate how environmental variables explain the seasonal variability of XCH$_4$ over Northern high latitude wetland areas, we needed to define case study regions that are both representative of wetland areas and exhibit seasonality in environmental variables. A general challenge in defining a case study area, is that one hand it has to be large enough to host a sufficiently representative set of concentration observations but on the other hand small enough so that the area is to some extent homogeneous when considering the emissions and sinks. After testing, we decided to concentrate on five areas over the Northern Eurasia. The areas are shown in Fig. 1 and are called Northern Finland, Southern Finland, Northern Siberia, Middle Siberia, and Southern Siberia. The borders of the case study areas were defined based on The Boreal-Arctic Wetland and Lake Dataset (BAWLD, Olefeldt et al., 2021). Figure 1 shows the case study areas over BAWLD total wetland fraction map. In addition, the latitude and longitude borders of the areas are listed in Table 1. The total wetland and wetland type fractions for each case study area are also listed in Table 1. Based on the map in Fig. 1 and Table 1, for the Siberian case study areas, the total wetland fraction is over 40% and for the Finnish case study areas it is over 20%. The main wetland type is fen for Northern Finland, and bog for Southern Finland and Middle and Southern Siberia. Northern Siberia is the only area where permafrost bog is the main wetland type and also where the permafrost bog fraction is significant. The border between the Northern and Middle Siberia case study regions was defined in such a way that it separates areas where permafrost bog or bog is the dominant bog type.

3.2 Time series gap filling and fitting of the seasonal cycle of XCH$_4$

Before applying gap filling and fitting the seasonal cycle of XCH$_4$, we collected all quality-flagged TROPOMI WFMD v1.8 data for each case study area, covering the period from January 2018 to April 2024. For each day, we calculated the regional daily median XCH$_4$, along with its standard deviation and the number of observations per day, based on all observations within the area for that day. To minimize the influence of potential outliers, the daily median was calculated only for days with more than three observations. This restriction excluded a few individual spring dates. After calculating the daily medians, we applied a Kalman filter for gap filling, and the seasonal cycle was fitted using NOAA's curve fitting routine (CCGCRV; Thoning et al. 1989; NOAA 2012). CCGCRV is a non-linear fitting routine, developed by Thoning et al. (1989) to smooth and separate the seasonal cycle and long-term trend of CO$_2$ from the Mauna Loa in situ measurements. CCGCRV fits the long-term trend with third order polynomial function and the seasonal cycle is modelled with harmonic functions;

$$y = a_0 + a_1 x + a_2 x^2 + \sum_{n=1}^{4} [a_{2n+1} \sin(2n\pi x) + a_{2n+2} \cos(2n\pi x)] \tag{1}$$

where the terms a_0, a_1, a_2 represent the trend components, while the summation term captures the seasonal variation through the sine and cosine functions. The function is fitted with linear least squares regression routine that also gives the covariance of the fitting parameters and therefore the uncertainty of the parameters estimated. The fitting process produces a constant seasonal cycle, and to account for interannual and short-term variations, the residuals are filtered (NOAA, 2012; Pickers and Manning, 2015). CCGCRV gives as output the fitted trend, harmonic seasonal cycle with no interannual variability and smoothed seasonal cycle, where the interannual and short term variations are included. When considering the seasonal cycle of methane, CCGCRV has been previously used, for example, to study the decreasing seasonal cycle of methane in the Northern high latitudes (Dowd et al., 2023) and the year-to-year anomalies of satellite observations of methane in tropical wetlands (Parker et al., 2018).

The fit for each individual day in the CCGCRV method can be described as a combination of the function fit, which represents the harmonic cycle without interannual variability, and the filtered residuals, which accounts for interannual and short-term variations. Similarly, the uncertainty of each component can be estimated by combining the variances of these different elements (NOAA, 2012). For example, the uncertainty of the smoothed seasonal cycle is calculated by combining the variances of the function fit and the residual filter:

$$\sigma_{\text{smooth}}^2 = \sigma_{\text{function}}^2 + \sigma_{\text{filter}}^2. \tag{2}$$

Likewise, the uncertainty of the trend can be determined by combining the variances of the polynomial fit and the filter (NOAA, 2012).

Pickers and Manning (2015) investigated the possible biases related to three different curve fitting programs, CCGCRV being one of them. Pickers and Manning (2015) concluded and generated general recommendations on the use of these curve fitting programs and their suitability for time series analysis. Based on these recommendations we considered CCGCRV suitable for our analysis, as it was recommended to in cases where the year-to-year anomalies or the magnitude or timing of the seasonal

cycle are studied. To avoid the limitations of CCGCRV related to missing observations, it was suggested by Pickers and Manning (2015) that the data are gap-filled before applying CCGCRV, as CCGCRV only interpolates over the gaps.

235 We experimented different gap filling methods and studied their effect on the seasonal cycle in the Middle Siberia. The methods tested included the interpolation that CCGCRV can perform on its own, as well as Kalman filtering. For the Kalman filter, we experimented with several different parameter settings. Based on our analysis, the timing and the shape of the harmonic cycle fitted by Eq. (1) were quite similar regardless of the gap-filling method. The main differences in the fitted cycles were related to the amplitude of the seasonal cycle, as the winter maximum often coincided with a winter data gap, and the

240 timing of this maximum also varied slightly between fits. Based on our tests, we decided to use the Kalman filter for gap filling, as it initially provided the lowest chi-squared values for the function fit and the smallest residual standard deviation. The Kalman filter settings were further optimized to minimize the chi-squared value and the residual standard deviation. The defined Kalman filter settings were kept similar for each case study area. For the analysis, the winter gap was excluded to avoid drawing conclusions from periods without observations. This, along with the effect and contribution of the gap-filling method

245 on the results, is discussed in Sect. 4.

After filling the data gaps using the Kalman filter, we applied CCGCRV to the gap-filled time series for each study region, and calculated the uncertainties of the smoothed seasonal cycles. Figure 2 shows an example of the XCH_4 daily medians, gap-filled values, the fitted smoothed seasonal cycle with its uncertainty, and the fitted trend for Middle Siberia. Similar figures for other case study areas can be found in Appendix A, specifically in Figs. A1, A2, A3 and A4.

250 To investigate the spring time seasonal minima and maxima of the XCH_4 seasonal cycle in relation to factors such as snowmelt, we needed to determine the dates of these minima and maxima, along with their uncertainty estimates. To calculate the uncertainty estimates, we utilized the fitted harmonic seasonal cycle and the parameters a_n provided by the CCGCRV fit (as shown in Eq. (1)), along with the uncertainty estimates derived from the covariance matrix using a Monte Carlo approach. We sampled 10,000 states of the fitted cycle and calculated the dates of the minima and maxima for each state using the find_peaks

255 function from the Python scipy.signal package. For each minimum and maximum, we computed the standard deviation across these 10,000 states and used these standard deviations as the uncertainty estimates for the results presented in Sect. 4. The distribution of the values around each individual minimum and maximum was found to be Gaussian, allowing us to use the computed standard deviation for each minimum and maximum reliably as an uncertainty estimate.

3.3 Gridding and averaging of environmental variables

260 As environmental datasets in this study, we used the SMOS freeze/thaw state (F/T), IMS snow state (snow), The Copernicus Global Land Service Snow Water Equivalent product (SWE), ERA 2 m temperature (T/2m), ERA5 soil temperature at layer 1 (T/soil), ERA5 volumetric soil water at layer 1 (soil W) and CH_4 loss by OH (OH). These datasets are described in detail in Sect. 2, where, for example, the spatial and temporal resolutions are provided for each dataset. Abbreviations in parentheses corresponding to the variable names used in Sect. 4.

265 All environmental data were initially collected for the case study areas, presented in Sect. 3.1, and daily mean values along with their standard deviations were calculated over the areas. The environmental data sets were not gap filled, as they consist
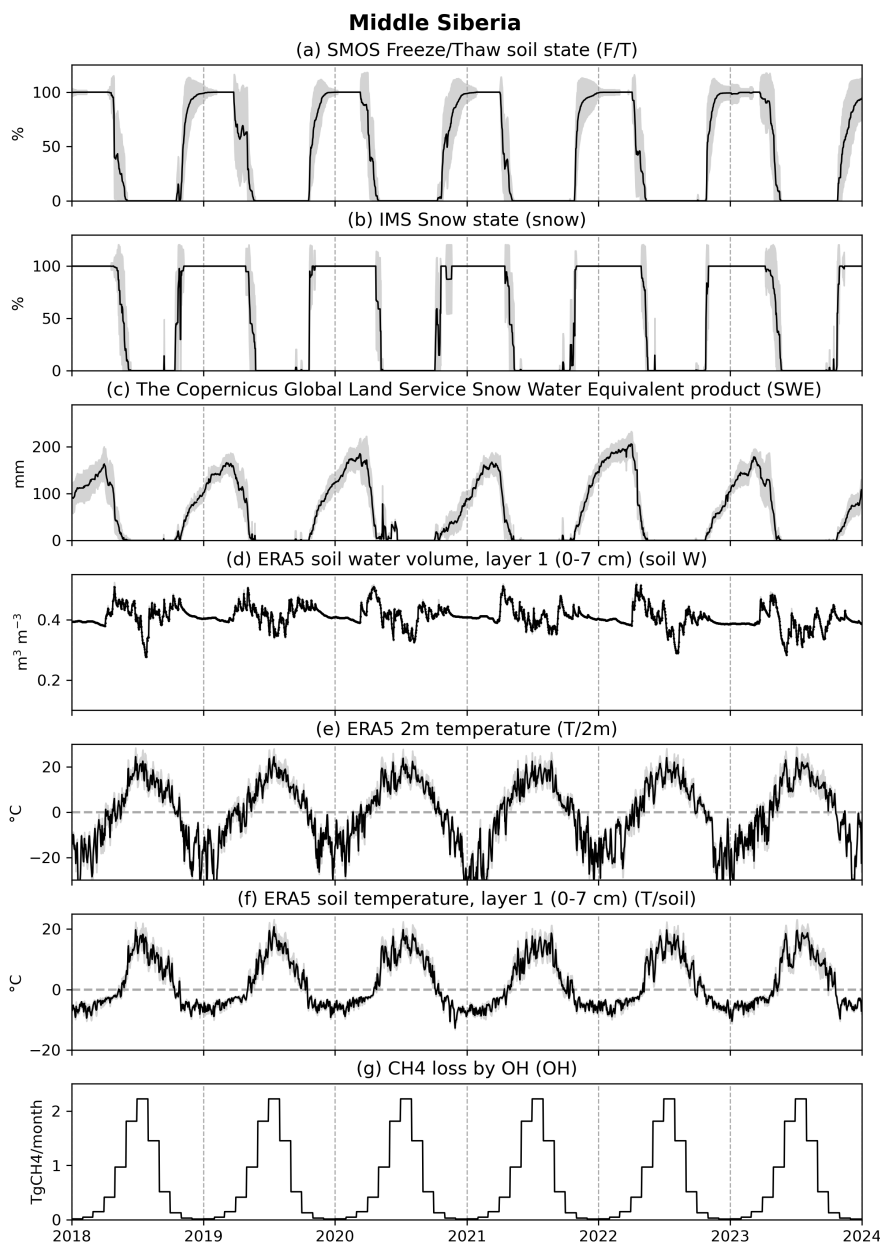
Figure 3. Black line shows the daily mean and the filled grey area the standard deviation of (a) soil freeze-thaw state, (b) snow cover state, (c) snow water equivalent, (d) layer 1 soil water volume, (e) 2 meter air temperature, (f) layer 1 soil temperature and (g) CH_4 loss by OH for Middle Siberia. The abbreviation mentioned in parentheses in the title of each subfigure is the abbreviation to be used for that environmental variable in the results.

of daily time series. Variations in the temporal and spatial resolution of the datasets required slight adjustments in averaging methods. SMOS F/T and IMS snow cover are categorical datasets: SMOS F/T has three categories, while IMS has two. For SMOS, we defined frozen as 1, partially frozen as 0.5, and thawed soil as 0. We then averaged these values across each case study area to obtain the regional mean soil freeze-thaw state. In the IMS snow cover data, snow-covered areas were defined as 1 and snow-free areas as 0, which allowed us to calculate the average snow cover fraction for each area. Snow water equivalent data has a daily temporal resolution, allowing us to calculate daily area-averaged values directly. For temperatures and soil water volume, derived from the ERA5 reanalysis data, hourly means were first calculated for each area, and from these hourly means, daily average temperatures and their standard deviations were computed. For the CH_4 loss by OH, there is no variability between years or a within month, as it has already been calculated for the 57°N–70°N latitude band, making it consistent regardless of the study area or year. Figure 3 illustrates the environmental time series for Middle Siberia. Similar figures for other case study areas can be found in Appendix B, specifically in Figs. B1, B2, B3, and B4.

The environmental datasets have relatively coarse spatial resolution, with the smallest grid cell size being 5 km in the SWE data and the largest being approximately 27.8 km in the ERA5 data along the longitude direction. The environmental variables in this case, such as snow cover or temperature, can vary significantly within these grid cells, depending on factors such as land type. For example, a transition from forest to wetland within a grid cell can lead to substantial variation in the variables. Therefore, in addition to the variability of environmental variables within the case study area, it is important to consider that there may also be variability within the grid cells.

For seasonal timing comparison (Sect. 4.2) we required estimates of the start and end dates of snow cover melt and beginning of decreasing SWE, along with their uncertainties. We defined the start of snow cover melt as the date when the IMS snow state over the area was below 0.9, and snow cover was considered completely melted when the mean snow cover fell below 0.1. To estimate uncertainties for these dates, we examined when the mean snow cover $\pm 1\sigma$ uncertainty fell below 0.9 for melt onset and below 0.1 for complete melt. This approach provided uncertainty bounds in both directions for the start and end dates of snow cover melt. To obtain the date when SWE begins to decrease significantly, we normalized the SWE data for each study area for each winter and identified the first day in spring when the normalized SWE was below 0.75; this day was used to represent the beginning of SWE decline. The uncertainties for this timing were estimated similarly to those for snow cover melt, by identifying the days when the mean SWE $\pm 1\sigma$ uncertainty dropped below 0.75.

3.4 Random forest feature importance and permutation importance

To study the links between the environmental variables and variability of XCH_4 on the daily level, we applied random forest regression method, using two different importance metrics: random forest feature importance (RFFI) and permutation importance (PI) methods, within the random forest model. Here, the environmental variables act as features in the random forest, allowing us to assess their individual contributions to XCH_4 variability. In general, random forest is a robust and well-established ensemble learning method that averages multiple decision trees to avoid overfitting and to improve the accuracy of the results (Breiman, 2001). RFFI and PI are importance metrics that can be used to evaluate the relationship between environmental variables and the seasonal variability of XCH_4. RFFI measures variable importance based on tree structure, while PI evaluates it by

shuffling values within the variable, assessing the resulting impact on model performance. By analysing these scores together we can study the connections of environmental variables and seasonal variability XCH$_4$ in more detail, as the scores provide different types of information and the calculated importance either can support each other or highlight some differences.

The first method, RFFI, measures how each variable contributes to the decision-making process within the random forest model. RFFI is normalized to provide a relative ranking of variable importance so that the sum of importance values over the variables is one. The second method, PI, describes the performance of the model when the values of each environmental variable are shuffled. PI directly measures the impact of each environmental variable on the random forest model's predictive accuracy, which provides additional information about the relevance of each environmental variable by showing how much the prediction error increases when a particular variable is disrupted. It is important to note that the calculated RFFI and PI importance values are not directly comparable as they measure different aspects and their units are different. Using both methods together allows for a more comprehensive understanding of variable importance by comparing the effects of different importance methods and settings on the results. Additionally, it should be noted that high correlations between environmental variables can influence the RFFI results, as highly correlated variables may share the importance assigned by the model, making it difficult to distinguish their individual contributions to the model. In contrast, PI is less sensitive to correlations as it measures the independent impact of each variable on model performance, although it may still be affected by the shared information problem in cases of highly correlated features. For this reason, it is also good to use two importance methods, as the environmental variables are usually correlated to some extent. The random forest model performance requires a large data volume; therefore, we collected data from all of the case study regions. The total number of daily median XCH$_4$ from all of the case study regions was 4935, distributed to Northern Finland, Southern Finland, Northern Siberia, Middle Siberia, Southern Siberia with 720, 715, 1118, 1134, 1248 daily medians, respectively.

We studied separately the relationship of environmental variables and the fitted seasonal cycle of XCH$_4$ (Fig. 2(b) red line), and the relationship of environmental variables and detrended daily XCH$_4$ medians (Fig. 2(b) blue dots) to estimate the potentially different drivers for the variability in different time scales. For both, we conducted the same methods: only those days when we had TROPOMI XCH$_4$ observations were considered. Therefore, the analysis and results can be considered to apply only to the spring-summer-fall period as we are missing XCH$_4$ values from winter time.

To obtain the results of this study we used scikit-learn Python module and its built-in methods and functions for fitting the model and to calculate RFFI and PI (Pedregosa et al., 2011). The random forest model was set up with 100 decision trees and trained using 80% of the available data, with the remaining 20% used for testing the model's performance. The model was implemented without pruning. We tested different numbers of trees, but the model's performance did not significantly improve as the number of trees increased. Given the relatively small size of the dataset it was important to keep the number of trees small enough. For the results presented in Sect. 4.1, the number of features to consider when determining the best split (parameter 'max_features') was set to 'sqrt', meaning the number of features considered at each split was the square root of the total number of features in the model. The choice of 'max_features' was based on a sensitivity analysis that assessed model performance and root mean square error (RMSE) using cross-validation. In addition to 'sqrt', we also tested with 'n_features", where all features are considered when determining the best split. The choice of the number of features had no effect on the

ranking of the feature importances, indicating robust identification of key drivers regardless of the model configuration. Model performance improved slightly with 'sqrt", increasing the model's coefficient of determination (R^2) from 0.840 to 0.851 for the seasonal cycle, and from 0.317 to 0.322 for daily medians. The RMSE decreased for the seasonal cycle from 8.05 ± 2.84 ppb to 7.93 ± 2.94 ppb, while it increased slightly for daily medians from 14.09 ± 1.21 ppb to 14.16 ± 1.17 ppb. Although the

340 changes in performance metrics were small when altering the 'max_features' parameter, 'sqrt' was chosen because it increases tree diversity, reduces the risk of overfitting, and generally improves model generalization. For permutation importance, we defined the number of reputations to be 50 to obtain a robust estimate of each variable's contribution.

To evaluate the uncertainty of RFFI and PI we fitted the random forest model 1000 times using different random seeds. The final feature importance values that are presented in the results in Sect. 4.1, were calculated as the average of these thousand

345 fits and the uncertainties of the importance values were estimated by calculating the standard deviation of the sample.

Among the environmental variables that we use in our analysis, the following were highly (i.e. correlation coefficient $|r| \geq$ 0.85) correlated: snow cover and snow water equivalent ($r = 0.89$), snow cover and soil freeze-thaw state ($r = 0.91$), snow cover and soil temperature ($r = -0.85$), snow water equivalent and soil freeze-thaw state ($r = 0.96$), 2 meter air temperature and soil temperature ($r = 0.93$), and soil temperature and OH ($r = 0.87$). These high correlations can mostly be explained by

350 physical mechanisms and are not surprising. It is important take these correlations into account, especially when analysing the RFFI results.

4 Results and discussion

4.1 Links between environmental variables and XCH$_4$

Our aim is to study the links between environmental variables and the seasonal variability of XCH$_4$ and to estimate the

355 potentially different drivers for the variability in different time scales. The time scales we consider include the fitted seasonal cycle, which captures the seasonal changes but cannot detect short-term variations or extremes, and day-to-day variability, which is more sensitive to small-scale atmospheric changes and can exhibit larger fluctuations than the seasonal cycle. In addition, we study the daily median – seasonal cycle difference, which describes how the daily value differs from the seasonal value and is used in our analysis to strengthen the results; the daily median – seasonal cycle can be thought in a way as methane

360 anoamaly respect to the seasonal cycle. The methane XCH$_4$ data used in this study (WFMD v.1.8) performs well compared to reference data sets across all seasons (Lindqvist et al., 2024), indicating its reliability in capturing both seasonal and daily variability across all available time periods. The mean daily median – seasonal cycle difference varied between the case study areas, ranging from 2.0 ppb to 3.9 ppb. This difference is generally highest during spring, when day-to-day variability peaks, with methane concentrations showing notably stronger low values on individual days (for example, Fig. 2 for the year 2018),

365 and, additionally, the concentration drops sharply from the winter maximum to the winter minimum (for example, Fig. 2 for the year 2022).

The analysis is performed by applying random forest regression method using RFFI and PI importance metrics. Figure 4 shows PI and RFFI of each studied environmental variable on the detrended XCH$_4$ daily medians ((a) and (b)), fitted XCH$_4$
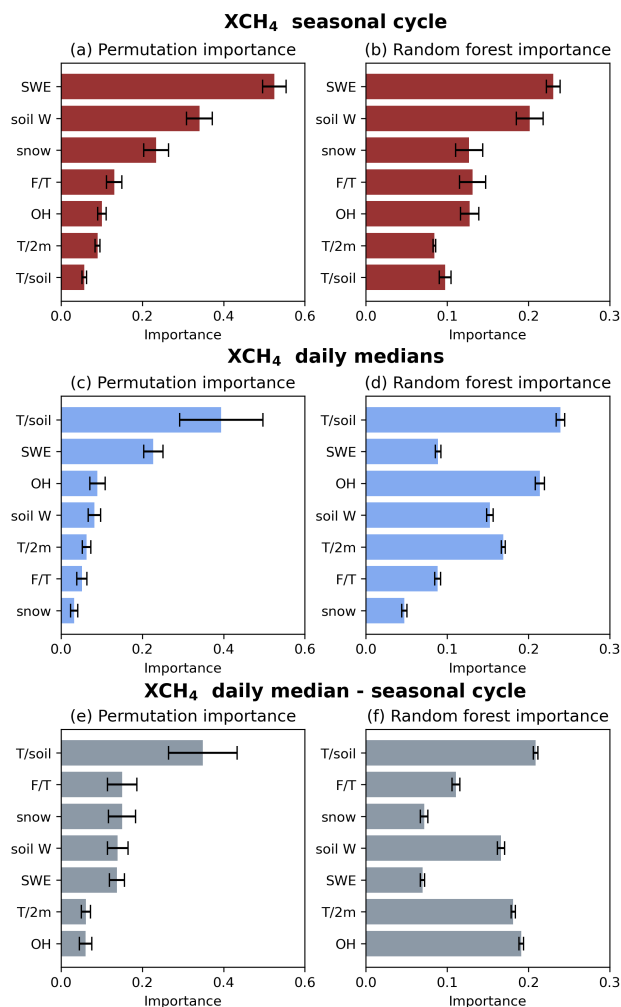
Figure 4. Permutation and random forest feature importance metrics for XCH$_4$ seasonal cycle ((a) and (b)), XCH$_4$ daily median ((c) and (d)), and XCH$_4$ daily median – seasonal cycle difference ((e) and (f)). The importances are ordered based on the permutation importance, the most important being the uppermost and the lowest being the least important. The importances are calculated as an average from 1000 random forest fits and the uncertainties (black lines) are the standard deviations of those fits.

seasonal cycle ((c) and (d)) and for daily median – seasonal cycle difference ((e) and (f)). The environmental variables are

370   ordered in the y-axis based on their PI rankings. Black line shows the uncertainty of the importance. Figure 5 shows the ranking of environmental variables based on their importance to different XCH$_4$ components; the higher bar signifying higher significance. Each colour represents each XCH$_4$ component and the shade of the colour is based on the used importance method.
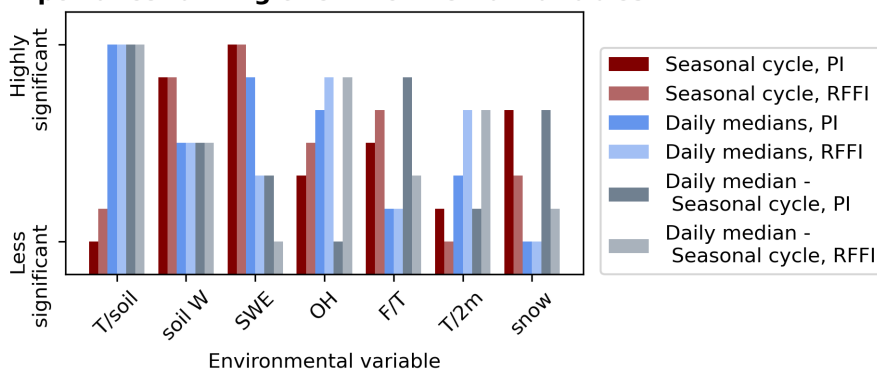
Figure 5. The ranking of environmental variables based on their importance to XCH_4 variability. The height of each bar represents the variable's rank: a higher bar indicates greater importance. Each colour indicates different XCH_4 component (blue: daily median; red: fitted seasonal cycle; grey: daily median – seasonal cycle difference) and the shade of the colour the used importance method (darker: PI; lighter: RFFI).

Based on Figs. 4 and 5, for the XCH_4 seasonal cycle, both PI and RFFI show somehow similar patterns, SWE and soil water volume being the most important environmental variables. The order of importance for soil freeze-thaw state, air temperature, snow cover, soil temperature and OH varies slightly between PI and RFFI but all of these variables are less significant than SWE and soil moisture according to both methods. For the XCH_4 daily medians and the difference between daily medians and the seasonal cycle, PI and RFFI produce somewhat similar results: according to both methods, soil temperature is the most important environmental variable for both XCH_4 variables. For PI, this is clearer than for RFFI, and the order of importance for other environmental variables differs between the methods. Based on RFFI, OH is the second most important for XCH_4 daily medians, while based on PI, it is SWE. According to PI, the importance of other environmental variables than soil temperature and SWE are minimal, while based on RFFI, each environmental variable has some effect. For the daily median – seasonal cycle difference, soil temperature is the most important variable based on both RFFI and PI. This is somewhat expected, as soil temperature was not significant for the XCH_4 seasonal cycle, but it was for the daily medians, and SWE was important for both. Interestingly, for the difference, the soil water volume, which was a significant factor in the seasonal cycle, does not appear as an important variable for the daily median – seasonal cycle difference.

However, the analysis also reveals that the RFFI results may not be as reliable for interpretation as those based on PI. As noted in Sect. 3.4, the correlation between environmental variables can affect their relative importance when considering RFFI, making it difficult to distinguish their individual contributions. This issue is particularly evident, for example, in the XCH_4 daily median results, where RFFI suggests that OH is the second most important variable, with an importance value very close to that of soil temperature (Fig. 4 (d)). In contrast, PI ranks OH as the third most important, with a clear difference in importance compared to soil temperature. According to correlation analysis, OH and soil temperature are highly correlated ($r = 0.87$), which leads to challenges in distinguishing their individual importance in the RFFI results. Given these concerns,

and considering the challenges RFFI faces when the features are correlated, we focus on the PI results and use RFFI results as
395   supporting information for variables that are not as strongly correlated. It should also be noted that due to the high correlation
of the variables, the PI values could still be affected to some (but to a much lesser) extent by the issue of shared information
between features (see Sect. 3.4).

The similarities and discrepancies between PI and RFFI importance scores suggest that, for XCH$_4$ seasonal cycle, the random
forest model performs relatively steadily, with SWE and soil water volume being the main drivers of the seasonal cycle's phase.
400   However, for the short-term XCH$_4$ variability, the model is less stable, indicating that the mechanisms behind daily variability
are more complex and that short-term environmental variability has little systematic impact in the total column. Nonetheless,
soil temperature plays clearly a large role in short-term variability. This difference between the seasonal cycle and daily median
results is consistent with the sensitivity analysis of the random forest model presented in Sect. 3.4, where it was found that
model's performance was stable across different configurations but was clearly better for seasonal cycle than for daily medians.

405   The driving factors and conditions of the seasonal variability of methane emissions from different land and vegetation types
has been previously widely studied with in situ measurements and modelled CH$_4$ fluxes and concentrations. As stated in
the introduction, the seasonal variability of the column-averaged dry-air mole fraction of methane is a combination of the
seasonality of CH$_4$ emissions and sinks, and transport patterns. Therefore, the results from local flux studies cannot be directly
compared to our findings, although fluxes influence the XCH$_4$ concentrations. Next, we will compare our results with previous
410   findings from in situ and model studies, and examine how the dependencies of methane on environmental variables identified
in those studies are reflected in our results.

East et al. (2024) studied the hemispheric differences and the drivers of the seasonality of methane concentrations based on
model simulations. They showed that in the Southern Hemisphere the seasonal cycle is smooth and driven by the OH sink but
the seasonal cycle in the Northern Hemisphere is asymmetric and has a sharp increase during summer. Based on their results
415   with chemical transport model, they found that the magnitude, latitudinal distribution and seasonality of wetland emissions are
critical for the seasonality of methane in the Northern Hemisphere as they determine the timing and magnitude of the summer
increase. Our findings further specify those of East et al. (2024), as our results print out the importance of soil water volume,
snow cover, and soil temperature; these variables are all important factors for methane production in high latitude wetlands,
either directly or indirectly, by influencing the soil water cycle and temperature.

420   Snow and frost require similar conditions, specifically temperatures below zero degrees Celsius. Moreover, they are closely
interconnected: snow acts as an insulating layer, influencing soil freezing and thawing. For methane emissions, snow plays an
important role as it slows down methane from entering the atmosphere from the soil. Snow also contributes to soil thawing,
as water from melted snow thaws the soil from above and increases the soil water volume. Studies that have carried out
measurements outside the growing season have mainly focused on quantifying fluxes during the cold season and comparing
425   them to annual emissions. However, only few studies have directly studied the relationship between snow and methane fluxes,
partly due to the difficulty in accessing in situ observation sites during the winter months. The cold season emissions can cover
a major part of the annual emissions, despite snow and soil frost (e.g, Zona et al. 2015; Rößger et al. 2022). The emissions
during the cold season are relatively stable, with a monthly distribution accounting 4–8% of the annual emissions (Rößger

et al., 2022). However, since the cold season lasts in some parts of high latitudes from early October to early May, a significant
amount of emissions is accumulated over this time period and therefore the cold season emissions are important to the annual
methane budget in these areas. As mentioned in Sect. 2.4, the quality of SMOS F/T product data near Russia is affected by
RFI interference. However, it was observed that in our case, the interference significantly impacted the data quality only for
the year 2023. Our earlier results, which did not yet include data from 2023, were consistent with the current findings. This
consistency suggests that the interference has not impacted our results, which is logical given the relatively low importance of
soil freezing (Fig. 4).

From the studies that have been directly investigating the connections between snow and methane, Mastepanov et al. (2013)
found that the springtime increase in CH_4 flux was strongly correlated with the date of snowmelt. Additionally, Rößger et al.
(2022) reported that earlier snowmelt and higher early summer temperatures in June has increased the early summer CH_4
fluxes in Siberian Tundra. Both Zona et al. (2015) and Rößger et al. (2022) showed a significant rise in methane emissions
over a wetland following the spring thaw, and then strong monthly emissions that lasted over the thaw season. They both
defined the seasons based on temperatures, either air or soil. Our results show that for the XCH_4 seasonal cycle, snow is a
more determining factor than for XCH_4 daily medians; the amount of snow determines the phase of the XCH_4 seasonal cycle
together with soil moisture. However, Mastepanov et al. (2013) and Rößger et al. (2022) examined the effects of snow on small,
well-defined land types, whereas in our study, the SWE data resolution is 5 km, approximately the same as the TROPOMI pixel
size. Despite this relatively small grid size, it still encompasses various land types with differing melting timings. Additionally,
when averaging across the entire case study area, further variability arises due to the diverse land types present. As shown
in Sect. 3.1 in Table 1, none of the areas had a total wetland fraction exceeding 50%, indicating that more than half of the
area consists of non-wetland types. In Section 4.2, we further address this uncertainty by calculating case study area specific
uncertainties.

The effect of soil moisture on methane emissions is a complex process, and the results are significantly influenced by fac-
tors such as wetland type or the time period (month, season, year) being studied. For example, Kittler et al. (2017) compared
methane emissions from a drained area to a more moist control area at moist tussock tundra that is located on Siberian per-
mafrost area. They showed that the annual amount of methane emissions is correlated with drainage; in the drained area, annual
methane emissions were lower than in the moist control areas. On the other hand, Zona et al. (2015) studied emissions from
the Alaskan tundra and showed that, at the driest sites, cold-season emissions dominated the annual emissions. Based on our
importance analysis, soil water volume, which describes soil moisture, is strongly linked to the seasonal variability of XCH_4.
However, its influence in the shorter-term variability is more complex, making it difficult to capture using simple statistical
measures, such as the Pearson correlation coefficient. This complexity may arise from relatively strong day-to-day variability in
soil moisture during the summer, as well as significant local variations, such as differences in soil types (e.g., Kittler et al. 2017
and their comparison between two adjacent areas). Since the environmental variables used in this study are relatively sparse
in spatial grid resolution and are then averaged over larger areas, there are inevitably many different land and wetland types
within each grid cell and within the case study area. Furthermore, the soil water volume in Layer 1 represents soil moisture
in the topsoil, and it is possible that methane emissions during the summer are more influenced by water table depth, which

changes more slowly than topsoil moisture. The Layer 1 was chosen because it represents the soil properties in the 0–7 cm layer, while Layer 2 represents the 7–28 cm depth, and we wanted to select the layer closest to the surface. Both layers were not chosen because their correlation was really close to one, which would have made the interpretation of PI and RFFI importance values more difficult. In permafrost areas, the active permafrost layer depth might also have an effect. To study the effect of soil moisture on XCH_4 at a more detailed level, it would likely be necessary to consider different soil types individually, permafrost areas, and the relationship between soil moisture and individual XCH_4 satellite observations. Additionally, spatially representative data on water table depth would be valuable, as methane emissions continue when the water table drops below the 7 cm depth observed in topsoil moisture, but they cease in deeply drained soils and turn into a methane sink. In permafrost regions, it would also be valuable to study the seasonal development of active layer depth, as it determines the thickness of the soil layer emitting methane. We tested the analysis using satellite-based soil moisture data (Dorigo et al., 2017), but the main issue was that it is not daily data, and there were significant data gaps during springtime. This prevented a comprehensive analysis with that data and was the reason to use ERA5 soil water volume instead.

Based on flux studies, it can be stated that during the growing season, there is a positive correlation between methane flux and soil temperature (e.g., Mastepanov et al., 2013; Howard et al., 2020; Kittler et al., 2017). This relationship is linked to microbiological activity, which is enhanced by higher soil temperatures, leading to increased methane emissions from wetlands. According to both PI and RFFI scores, soil temperature is the most important factor influencing the detrended XCH_4 daily medians, although for PI, the uncertainty range is high. Nevertheless, soil temperature remains the most important within this range. Zona et al. (2015) showed that when the soil temperature is below zero, CH_4 emissions are small, but as the soil temperature increases toward zero and above, methane emissions begin to rise, with the highest emissions occurring during July and August. Similarly, Kittler et al. (2017) showed that emissions peak during July and August and follow the temperature. We examined the correlation between soil temperature and the detrended XCH_4 daily median for each month separately and found that, during the period from May to August, the correlation between the daily mean soil temperature and the detrended XCH_4 daily median was moderate, with Pearson correlation coefficients of 0.34, 0.39, 0.48, and 0.32, respectively. During the other months, the correlation was not larger than 0.3, but in April and October, it ranged between 0.2 and 0.3. Although the Pearson correlation coefficients are relatively low, our results regarding the significance of soil temperature are consistent with previous research, which shows that temperature affects methane emissions. We observe this in the XCH_4 data, and the low correlations may be attributed to the fact that methane emissions may respond with a delay to changes in temperature. The random forest model, which can incorporate time lags, likely explains why, despite the low correlations, soil temperature still shows significant importance in the model.

OH became a significant factor based on the RFFI importance score for XCH_4 daily medians, likely due to its high correlation with soil temperature (r = 0.87). As noted in Sect. 3.4, highly correlated variables may share the assigned importance in the random forest model when using RFFI. However, PI importance score is not as sensitive as RFFI for this sharing effect, and in the PI scores, OH ranks as the third most important factor, though it has significantly less influence compared to soil temperature or SWE (Figs. 4 and 5). In addition, it should be noted that we used monthly zonal mean CH_4 loss values from TM5, calculated for the latitude zone 57°N–70°N (see Sect. 2.6). The method used is a simplification; we assumed that the
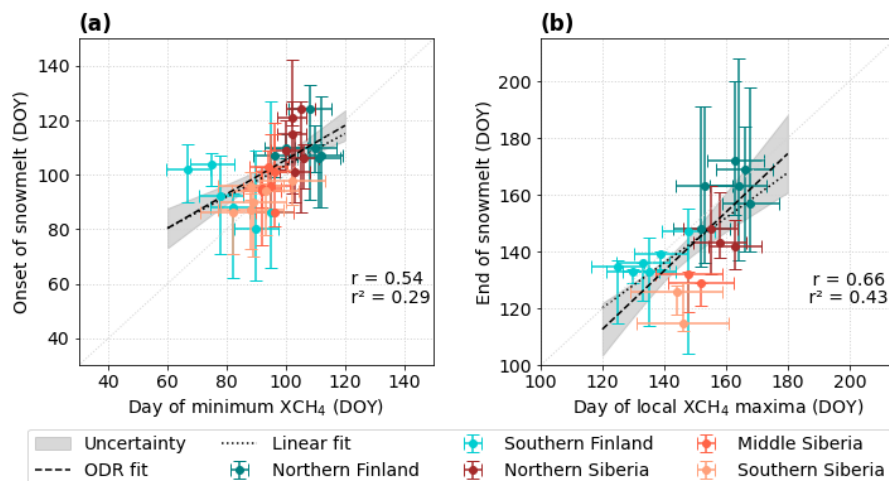
Figure 6. Scatter plots show (a) onset of snowmelt (y-axis) versus the day of the year when the XCH₄ seasonal cycle reaches its minimum (x-axis), and (b) the end of snowmelt (y-axis) versus the day of the local maxima in XCH₄ (x-axis). Both figures also display the one-to-one line in gray dots, a linear fit as a black dotted line, and an Orthogonal Distance Regression (ODR) fit as a black dashed line. The ODR fit accounts for uncertainties in both directions, with all uncertainties calculated based on the data.

large-scale OH loss is sufficient to examine the variability of XCH₄ in this study. This is based on the assumption that OH
500   loss would not vary significantly spatially between the study areas at a monthly resolution. However, this assumption does
not take into account that OH concentrations depend on factors such as the amount of UV radiation and humidity (Lelieveld
et al., 2016; Zhao et al., 2019), and therefore, it has also shorter-term and interannual variability. As we concentrate on the
Northern high latitudes, we are dealing with spectrally and temporally variable surfaces, particularly seasonal snow cover,
which can influence OH levels due to varying UV reflection from the surface. For instance, Prinn et al. (2001) presented that
505   during El Niño–Southern Oscillation (ENSO) events, increased cloud cover corresponds to lower OH concentrations, likely
due to reduced UV radiation near the surface. Consequently, snow cover may impact not only methane fluxes but also the
atmospheric methane sink indirectly. A more detailed and deeper evaluation the effectiveness of the OH sink would require
more accurate OH estimation or the use of new proxies to demonstrate small-scale variations in OH concentrations. Given
that the lifetime of OH is very short, typically approximately one second, and it is highly sensitive to disturbances in both its
510   sources and sinks (Wolfe et al., 2019) it is challenging to measure OH concentrations or reliably model its concentration spatial
variability in the atmosphere. Until now, atmospheric measurements of methyl chloroform have often been used as a proxy
for OH concentration; however, this approach is becoming increasingly difficult as methyl chloroform concentrations decline
(Zhang et al., 2018).

4.2 Seasonal timing of XCH$_4$ minima and maxima in relation to snow

515   Snow influences wetland methane emissions in multiple ways, for instance, it acts as an insulating layer for the soil, affecting soil temperatures and freezing processes, thereby directly impacting methane production in the soil. Snow also slows down the methane emissions from entering to the atmosphere from the soil. In spring, as snow melts, a pulse of methane emissions is often observed, resulting from methane that accumulated beneath the snow and ice during winter being released after the snowmelt and soil melt (Rinne et al., 2007). Additionally, soil moisture is closely linked to snowmelt in spring; Figs. B3, 3, and

520   B4 show that in the Siberian case study areas, soil water volume typically increases sharply to a distinct peak during the period between the onset and the end of snowmelt. This increase in soil water volume is linked directly to melting snow. In Northern and Southern Finland, this pattern is less distinct, though similar features can still be observed to some extent (Figs.B1 and B2).

   Our results in Sect. 4.1 showed that the seasonal cycle of XCH$_4$ is also influenced by snow. To further investigate the

525   temporal connection between snow and the seasonal cycle of XCH$_4$, we focused on spring, particularly in the minimum XCH$_4$ in early spring and the local maxima in late spring or early summer, along snowmelt. The focus on spring was chosen because the annual maximum often coincides with time when TROPOMI observations are not possible, and the onset of snow cover frequently falls within this timeframe (Fig. C1), complicating the analysis. The impact of the winter gap on our analysis and the added value of increasing satellite observations during the winter gap in XCH$_4$ data are discussed in more detail at the

530   end of this section. For the analysis, we defined the end of snowmelt based on snow cover, rather than SWE, because it is a simpler method for determination, and in SWE time series, it is observed that significant amounts of snow may still fall after SWE approaches zero, for example, in Fig. 3(c) in the spring of 2020. When determining the end of snowmelt based on snow cover, these situations were more precisely defined. The onset of snowmelt, however, must be defined through the start of SWE reduction, as SWE begins to decrease much earlier than snow cover (Fig. C1). Threshold-based methods for defining the onset

535   and end of snowmelt are described in Sect. 3.3.

   The seasonal cycle of XCH$_4$ reaches its minimum in early spring and its maximum during the autumn or winter. Toward the end of spring, in certain years, local minima and maxima in the XCH$_4$ cycle are observed across specific case study areas, coinciding with the timing of snowmelt (Fig. C1). Figure 6 shows (a) the day of minimum XCH$_4$ relative to onset of snowmelt, and (b) the day of local maxima in XCH$_4$ compared to the end of snowmelt. Both plots include a linear fit, represented by a

540   dotted line, and an Orthogonal Distance Regression (ODR) fit, indicated by a dashed line. The ODR approach accounts for uncertainties in both the x and y directions. Both figures also display the Pearson correlation coefficient r and the coefficient of determination r^2. Uncertainties related to the timing of snowmelt and the phase of the XCH$_4$ seasonal cycle are calculated as presented in detail in Sections 3.2 and 3.3.

   Based on Fig. 6(a), the onset of snowmelt correlates with the day of the XCH$_4$ minimum, within uncertainties. However,

545   in the Southern Finland case study area, a few outliers are observed, specifically in the springs of 2020 and 2021 (Fig. 6(a)), when SWE showed a gradual decline without a clear, rapid drop, and substantial variability was present within the region (Fig. C1). The correlation between the onset of snowmelt and the day of minimum XCH$_4$ is moderate, with a correlation coefficient

of 0.54. When the two Southern Finland outlier years are excluded, however, the correlation strengthens substantially, with a coefficient of 0.74. The correlation between the day of the local maxima in XCH_4 and the end of snowmelt is moderately strong, with a Pearson correlation coefficient of 0.66. Both the linear and ODR fits are close to the 1:1 line, suggesting that the local maxima in XCH_4 generally occur around the time when the snow cover has fully melted.

In situ and modeling studies have mainly focused on the effect of soil freeze and thaw on methane emissions rather than on the impact of snow (e.g., Bao et al., 2021; Tenkanen et al., 2021). Based on previous studies, we were not able to draw clear conclusions regarding whether the coinciding of onset of snowmelt and the day of minimum XCH_4 is a result of each other. This uncertainty originates from limited knowledge about the amount of methane released during the early stages of snowmelt, when snow cover persists and the soil may still be frozen. The correlation between the day of local maxima in XCH_4 and the end of snowmelt is likely related to the connections between snow and methane, as presented in Sect. 4.1, where we referenced, for example, Mastepanov et al. (2013), who showed a strong correlation between the springtime increase in CH_4 and the date of snowmelt. In addition, Rinne et al. (2007) observed emission pulse during intense melting.

Although our importance analysis (Sect. 4.1) did not show that the loss of CH_4 due to the OH sink significantly affects the seasonal variability of XCH_4, Fig. C1 shows that the day of the local XCH_4 minimum often coincides with or occurs in July, when the CH_4 loss by OH is at its maximum (e.g., Fig. 3). When considering methane concentrations in high-latitude northern wetland areas, wetland methane emissions are most intense during the summer and growing season, while the the effect of OH sink in reducing methane concentrations is also at its highest. These effects essentially counteract each other. Although we were not able to directly observe or demonstrate this opposing influence from our results, it should still be considered when interpreting the findings. This also highlights the importance of incorporating more accurate OH fields or utilizing new proxies for OH, as discussed in Sect. 4.1, to enable a more precise analysis.

Bao et al. (2021) showed that the hourly mean emissions during spring thaw are lower than those during autumn freeze at high-latitude tundra sites. Additionally, the mean duration of spring thaw is typically less than a month, whereas autumn freeze lasts nearly two months. Since the effects of spring snowmelt are evident in the seasonal cycle of XCH_4 based on our analysis, it is reasonable to expect that the impact of autumn snow onset or soil freeze could also be detectable if we had the necessary observations. Based on Fig. C1, the winter gap begins between late October and mid-November and ends between mid-February and late March, depending on the year and case study area. The winter gap occurs because Northern regions experience very large solar zenith angles (SZA) during this period, with a period of no sunlight at all in areas above the Arctic Circle. The interannual variation in the winter gap duration is mostly driven by cloud cover and other meteorological conditions. These winter challenges are similar to what is expected for the upcoming missions, e.g Copernicu's Sentinel-5, CO2M, and GOSAT-GW. Consequently, reducing the winter gap and analyzing the effect of autumn freeze on XCH_4 remains a particularly challenging task. However, for instance, methane observations in the thermal-infrared range could be used to address this, especially if combined with data from current shortwave infrared observations, or active observations (e.g. upcoming MERLIN mission).

5   Conclusions

Studies directly utilizing GHG satellite observations provide valuable information to complement inversion results and offer new insights that can ultimately help reduce uncertainties in the global methane budget while improving our understanding of the increasing and variable trends in methane concentrations. To deepen our knowledge of the factors directly influencing

585   observed methane concentrations, this study investigated the dominant environmental variables that explain the seasonal variability of column-averaged methane. Based on previous in situ measurement based studies, we focus our analysis on snow, soil freeze and thaw, temperature, soil moisture and the impact of the OH sink. Based on our results, we further study the connections between the snowmelt and the phase of the seasonal cycle of XCH_4. Our analysis covers the period from 2018 to 2023 and focuses on five case study areas, including two in Finland and three in Siberia.

590   Our results suggest that the main drivers of the seasonal variability of column-averaged methane (XCH_4) over Northern high latitude wetland areas are soil moisture and snow, especially snow water equivalent. During the period when the soil is thawed, the main driver of day-to-day variability in XCH_4 is soil temperature. Other environmental variables considered in this study showed some effect on the seasonal cycle and day-to-day variability of XCH_4, but their influence was less significant compared to snow and soil moisture. These findings are based on satellite data analysis and cover much larger areas than in

595   situ measurements but still the results align with and are further validated by previous in situ and model studies.

Our analysis reveals that the phase of the XCH_4 seasonal cycle is closely linked to snowmelt timing. Specifically, the minimum in XCH_4 occurs around the onset of snowmelt, and the local maxima in XCH_4 coincide with the end of snowmelt, with Pearson correlation coefficients of 0.54 and 0.66, respectively. While we cannot conclusively attribute the increase in XCH_4 between the minimum and local maxima solely to the reduction in snow cover, the timing of these events appears to be

600   strongly correlated, likely due to the insulating effect of snow while it remains on the ground, and then the subsequent water entering the soil as snow begins to melt. Overall, our findings suggest that XCH_4 observations can be used to study the seasonal variability of methane on a large scale.

Our analysis focused exclusively on spring because the onset of snowfall in autumn coincides with the beginning of the winter gap in satellite methane observations, making it challenging to reliably study the seasonal cycle of XCH_4 during a

605   period for which we have no data. Obtaining observations from autumn and winter would be crucial to determine whether we can detect the onset of freezing and snow cover from the XCH_4 seasonal cycle. Additionally, accurately quantifying the amplitude of the XCH_4 seasonal cycle is important, as it is directly linked to the magnitude of CH_4 fluxes. In addition to studying the emissions, the analysis of the OH sink could be improved and better understood, particularly concerning day-to-day variability and the impact of the summer maximum on methane concentrations in conjunction with strong emissions. This

610   could be done, for example, by studying and applying potential new proxies to describe the effectiveness of the OH sink. This study demonstrates how the combination of different satellite, and model, datasets can be used to investigate the underlying physical processes driving environmental phenomena.

Data availability. The WFMD XCH_4 data is available at https://www.iup.uni-bremen.de/carbon_ghg/products/tropomi_wfmd/. IMS snow cover data is available at https://noaadata.apps.nsidc.org/NOAA/G02156/. The Copernicus Global Land Monitoring Service SWE product is

615 available at https://land.copernicus.eu/en/products/snow/snow-water-equivalent-v1-0-5km#download. ERA5 2 m temperature, soil temperature and soil water volume at layer 1 are available at https://cds.climate.copernicus.eu/cdsapp#!/dataset/reanalysis-era5-single-levels?tab= overview.
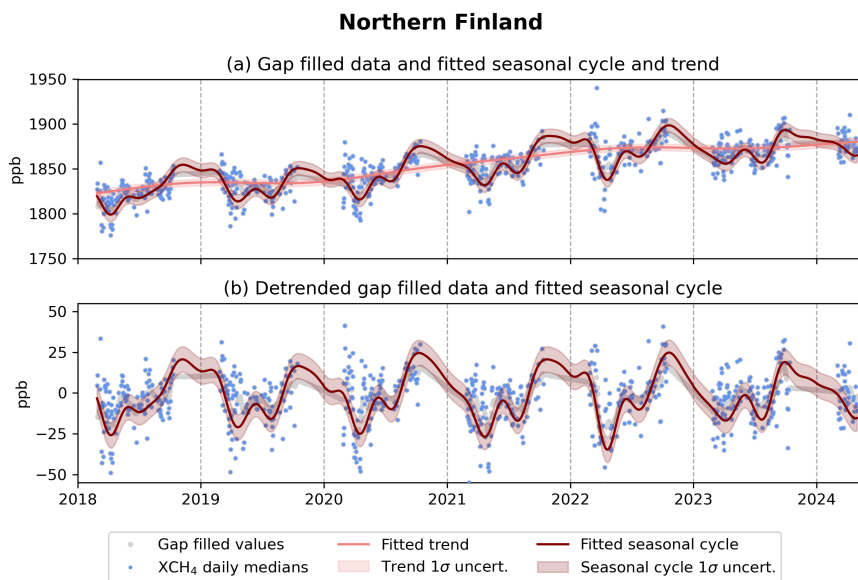
Figure A1. (a) TROPOMI WFMD daily median XCH$_4$ (blue dots), gap-filled XCH$_4$ values (grey dots) and fitted seasonal cycle and trend, and their uncertainties (red and shaded red) for Northern Finland. (b) shows the same for the detrended time series.

Appendix A: XCH$_4$ time series and fitted seasonal cycles
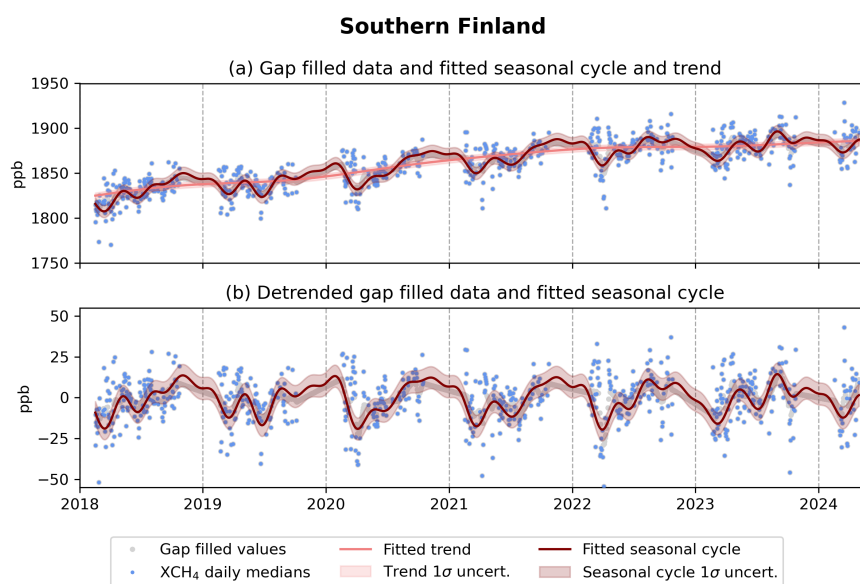
Figure A2. (a) TROPOMI WFMD daily median XCH$_4$ (blue dots), gap-filled XCH$_4$ values (grey dots) and fitted seasonal cycle and trend, and their uncertainties (red and shaded red) for Southern Finland. (b) shows the same for the detrended time series.
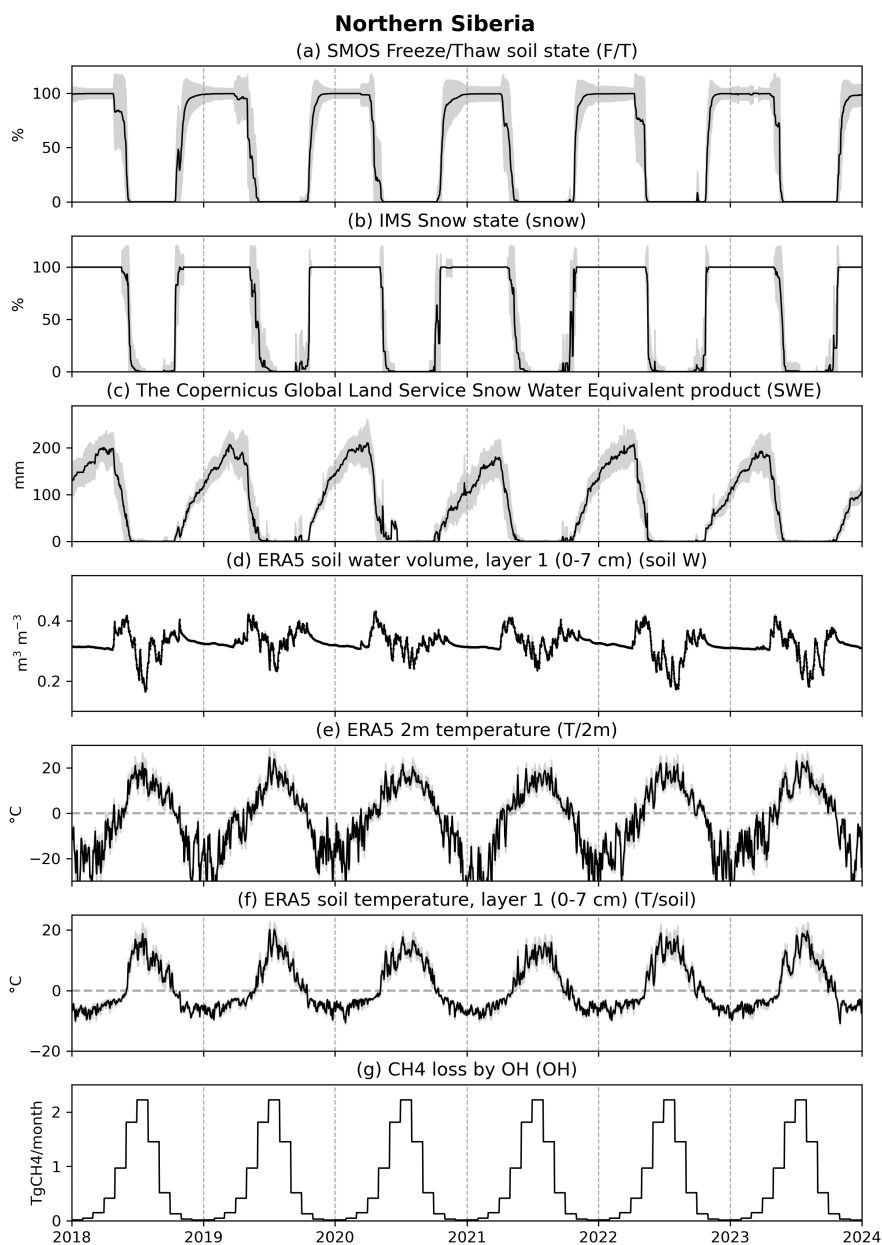
Figure A3. (a) TROPOMI WFMD daily median XCH$_4$ (blue dots), gap-filled XCH$_4$ values (grey dots) and fitted seasonal cycle and trend, and their uncertainties (red and shaded red) for Northern Siberia. (b) shows the same for the detrended time series.
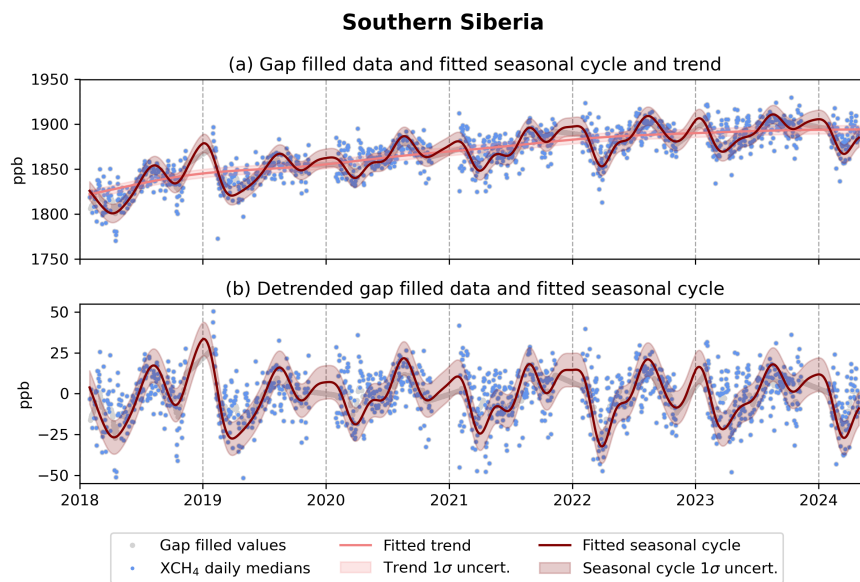
Figure A4. (a) TROPOMI WFMD daily median XCH$_4$ (blue dots), gap-filled XCH$_4$ values (grey dots) and fitted seasonal cycle and trend, and their uncertainties (red and shaded red) for Southern Siberia. (b) shows the same for the detrended time series.
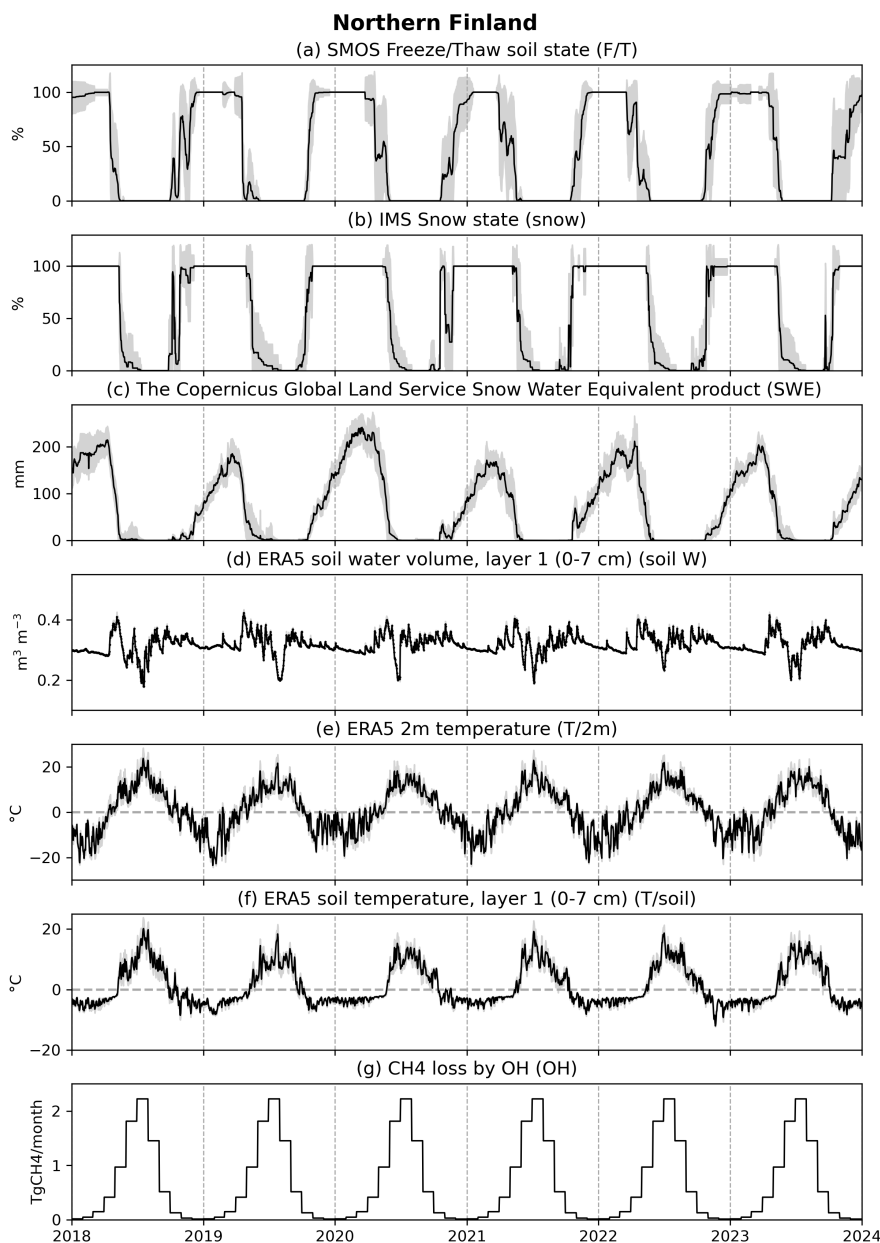
Figure B1. Black line shows the daily mean and the filled grey area the standard deviation of (a) soil freeze-thaw state, (b) snow cover state, (c) snow water equivalent, (d) layer 1 soil water volume, (e) 2 meter air temperature, (f) layer 1 soil temperature and (g) CH$_4$ loss by OH for Northern Finland.

Appendix B: Environmental time series
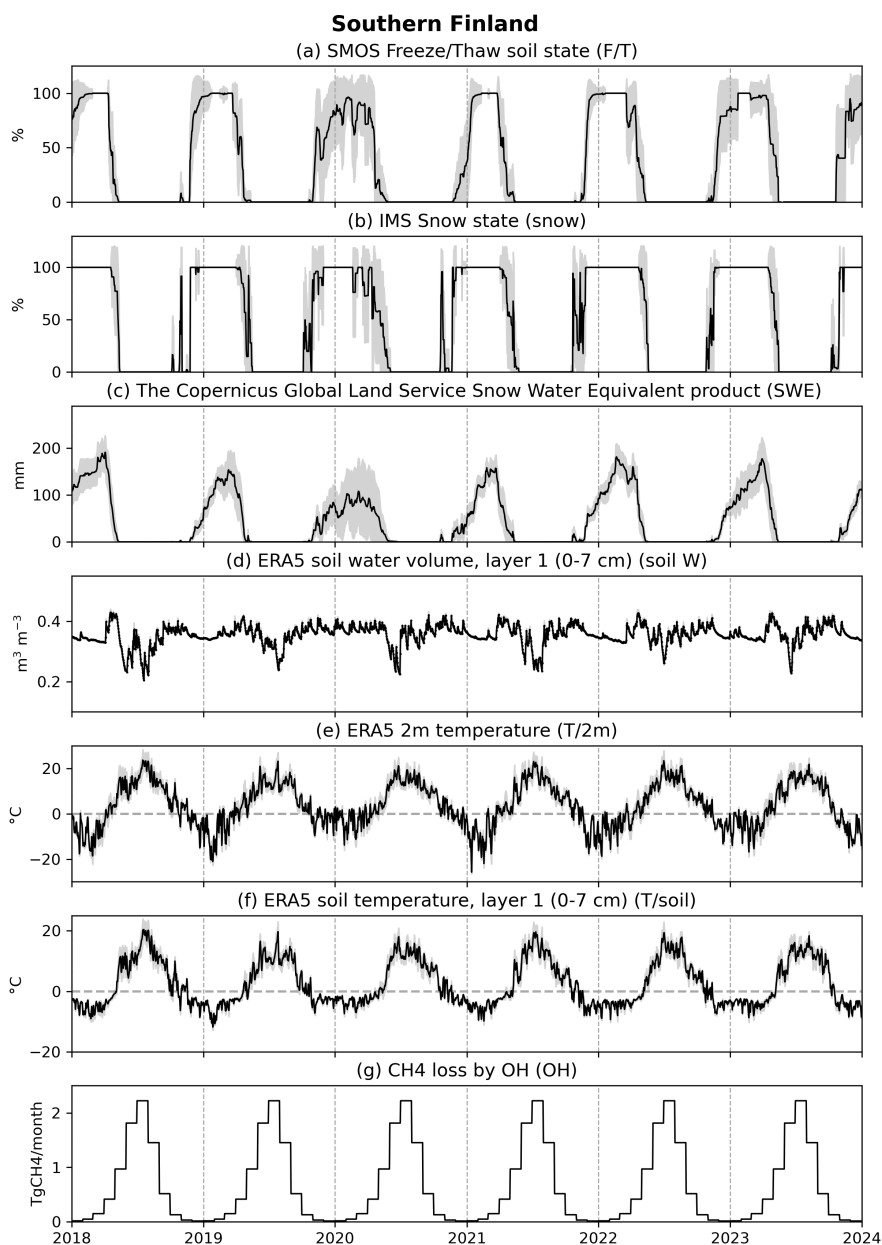
Figure B2. Black line shows the daily mean and the filled grey area the standard deviation of (a) soil freeze-thaw state, (b) snow cover state, (c) snow water equivalent, (d) layer 1 soil water volume, (e) 2 meter air temperature, (f) layer 1 soil temperature and (g) CH_4 loss by OH for Southern Finland.
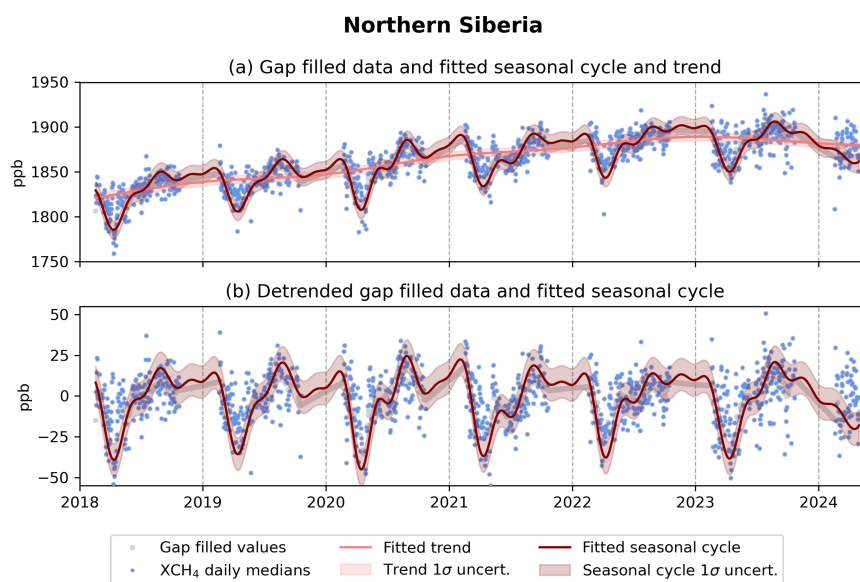
Figure B3. Black line shows the daily mean and the filled grey area the standard deviation of (a) soil freeze-thaw state, (b) snow cover state, (c) snow water equivalent, (d) layer 1 soil water volume, (e) 2 meter air temperature, (f) layer 1 soil temperature and (g) CH$_4$ loss by OH for Northern Siberia.
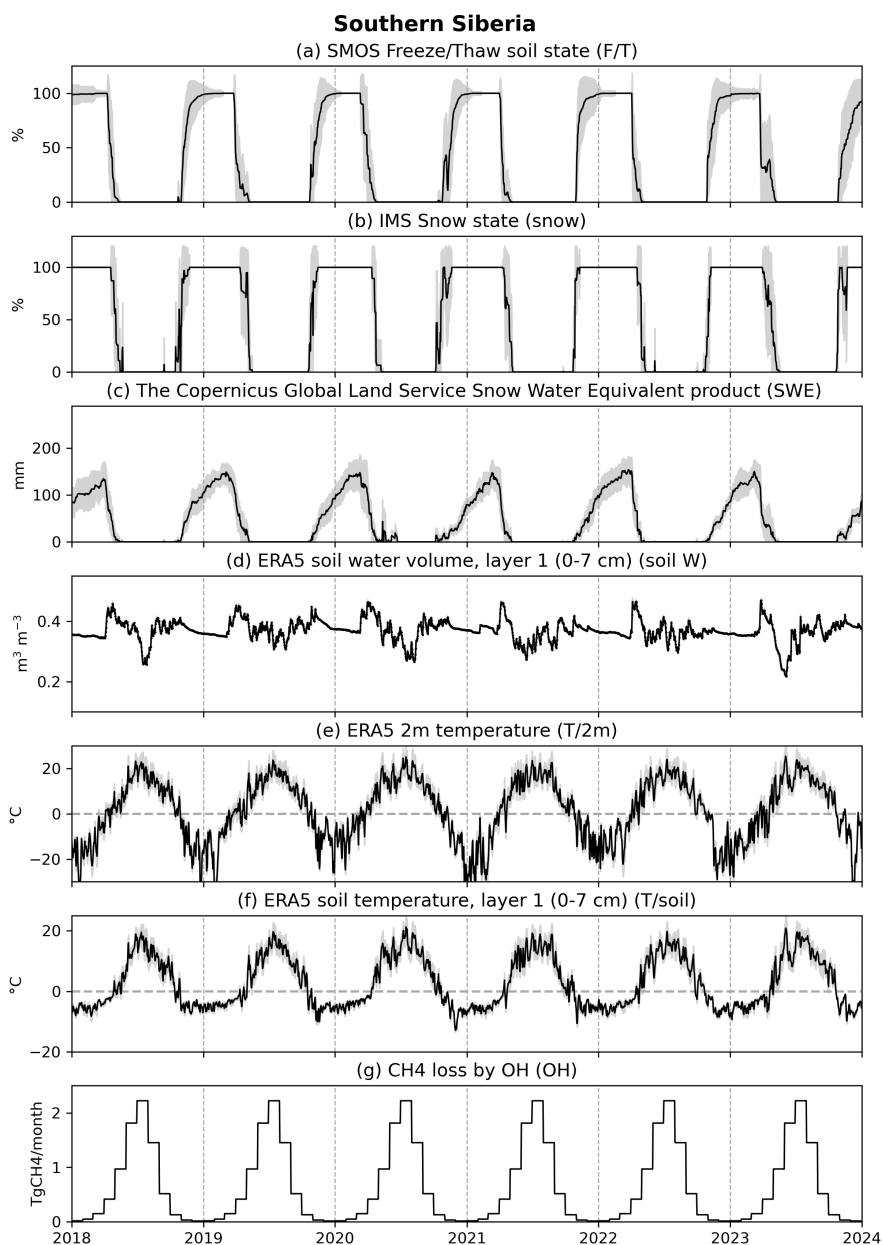
Figure B4. Black line shows the daily mean and the filled grey area the standard deviation of (a) soil freeze-thaw state, (b) snow cover state, (c) snow water equivalent, (d) layer 1 soil water volume, (e) 2 meter air temperature, (f) layer 1 soil temperature and (g) CH_4 loss by OH for Southern Siberia.
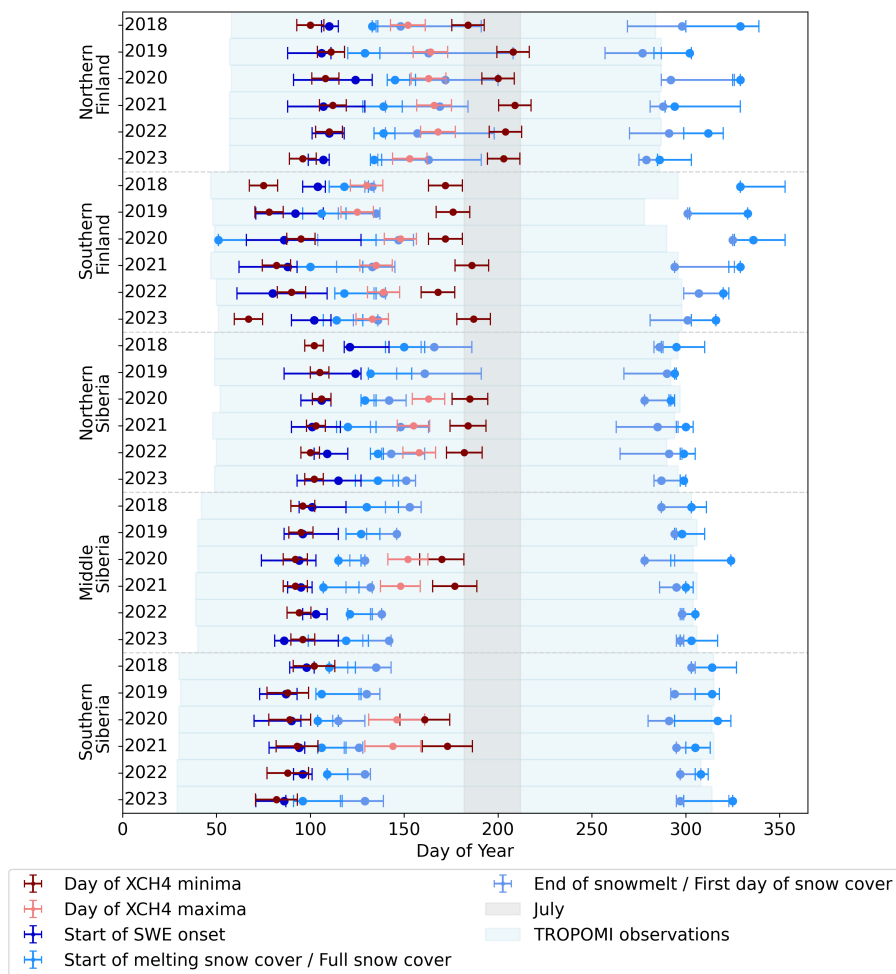
Figure C1. Snow melt and start of snow accumulation, and day XCH$_4$ minimas anx maximas time series

620 **Appendix C: Day of year time series**

Author contributions. E.K. and H.L. participated on the conceptualization of the study. E.K. prepared and performed the data processing, analysis, original draft preparation and the visualizations for the manuscript. H.L. participated in the draft preparation and supervision. J.T., J.P. and T.A. advised in the analysis and A-M. S. advised on the analysis of OH sink. A.T. processed the CH_4 loss by OH data and wrote it's data description. K.R. provided the SMOS F/T data. K.L. provided the SWE data. M. B. and O.S. provided the TROPOMI WFMD data. All

625   authors read and provided comments on the manuscript.

Competing interests. The authors declare that they have no conflict of interest.

Acknowledgements. FMI team acknowledges funding from the European Space Agency projects MethEO (4000125046/18/I-NB), MethaneCAMP (4000137895/22/I-AG), AMPAC-Net (AO/1-10901/21/I-DT), SMOS L3 Freeze/Thaw L3 Data Service (4000124500/18/I-EF), and ESA SMOS ESL2020+ (4000130567/20/I-BG)

630   In addition, FMI team acknowledges funding from the Research Council of Finland, through WINMET project (350184), ACCC - Flagship of The Atmosphere and Climate Competence Center (357904), FAME - Flagship of Advanced Mathematics for Sensing, Imaging and Modelling (359196), and The Centre of Excellence of Inverse Modelling and Imaging (353082).

E.K. acknowledges funding from the Tiina and Antti Herlin Foundation (Projects 20180222 and 20190003).

K.R. acknowledges funding from the Research Council of Finland Academy, through Research Fellowship project EMonSoil (364034).

635   The University of Bremen team acknowledges funding from ESA via project GHG-CCI+ (ESA contract no. 4000126450/19/I-NB) and the Bundesministerium für Bildung und Forschung within its project ITMS (grant no. 01 LK2103A). The TROPOMI/WFMD retrievals were performed on HPC facilities funded by the Deutsche Forschungsgemeinschaft (grant nos. INST 144/379-1 FUGG and INST 144/493-1 FUGG)

This publication contains modified Copernicus Sentinel data (2018–2024). Sentinel-5 Precursor is an ESA mission implemented on

640   behalf of the European Commission. The TROPOMI payload is a joint development by ESA and the Netherlands Space Office (NSO). The Sentinel-5 Precursor groundsegment development has been funded by ESA and with national contributions from the Netherlands, Germany, and Belgium.

We used an AI language model (ChatGPT) to support correcting the grammar of this manuscript.

References

645 Al Bitar, A., Mialon, A., Kerr, Y. H., Cabot, F., Richaume, P., Jacquette, E., Quesney, A., Mahmoodi, A., Tarot, S., Parrens, M., Al-Yaari, A., Pellarin, T., Rodriguez-Fernandez, N., and Wigneron, J.-P.: The global SMOS Level 3 daily soil moisture and brightness temperature maps, Earth System Science Data, 9, 293–315, https://doi.org/10.5194/essd-9-293-2017, 2017.

Bao, T., Xu, X., Jia, G., Billesbach, D. P., and Sullivan, R. C.: Much stronger tundra methane emissions during autumn freeze than spring thaw, Global Change Biology, 27, 376–387, https://doi.org/https://doi.org/10.1111/gcb.15421, 2021.

650 Barré, J., Aben, I., Agustí-Panareda, A., Balsamo, G., Bousserez, N., Dueben, P., Engelen, R., Inness, A., Lorente, A., McNorton, J., Peuch, V.-H., Radnoti, G., and Ribas, R.: Systematic detection of local CH_4 anomalies by combining satellite measurements with high-resolution forecasts, Atmospheric Chemistry and Physics, 21, 5117–5136, https://doi.org/10.5194/acp-21-5117-2021, 2021.

Berchet, A., Pison, I., Chevallier, F., Paris, J.-D., Bousquet, P., Bonne, J.-L., Arshinov, M. Y., Belan, B. D., Cressot, C., Davydov, D. K., Dlugokencky, E. J., Fofonov, A. V., Galanin, A., Lavrič, J., Machida, T., Parker, R., Sasakawa, M., Spahni, R., Stocker, B. D., and

655 Winderlich, J.: Natural and anthropogenic methane fluxes in Eurasia: a mesoscale quantification by generalized atmospheric inversion, Biogeosciences, 12, 5393–5414, https://doi.org/10.5194/bg-12-5393-2015, 2015.

Breiman, L.: Random Forests, Machine Learning, 45, 5–32, https://doi.org/10.1023/A:1010933404324, 2001.

Bridgham, S. D., Cadillo-Quiroz, H., Keller, J. K., and Zhuang, Q.: Methane emissions from wetlands: biogeochemical, microbial, and modeling perspectives from local to global scales, Global Change Biology, 19, 1325–1346, https://doi.org/https://doi.org/10.1111/gcb.12131,

660 2013.

Brühl, C. and Crutzen, P. J.: MPIC Two-dimensional model, NASA Ref. Publ., 1292, 103–104, 1993.

Buchwitz, M., de Beek, R., Burrows, J. P., Bovensmann, H., Warneke, T., Notholt, J., Meirink, J. F., Goede, A. P. H., Bergamaschi, P., Körner, S., Heimann, M., and Schulz, A.: Atmospheric methane and carbon dioxide from SCIAMACHY satellite data: initial comparison with chemistry and transport models, Atmospheric Chemistry and Physics, 5, 941–962, https://doi.org/10.5194/acp-5-941-2005, 2005.

665 CATDS: CATDS-PDC L3TB - Global polarised brightness temperature product from SMOS satellite, https://doi.org/10.12770/6294e08c-baec-4282-a251-33fee22ec67f, 2022.

Dorigo, W., Wagner, W., Albergel, C., Albrecht, F., Balsamo, G., Brocca, L., Chung, D., Ertl, M., Forkel, M., Gruber, A., Haas, E., Hamer, P. D., Hirschi, M., Ikonen, J., de Jeu, R., Kidd, R., Lahoz, W., Liu, Y. Y., Miralles, D., Mistelbauer, T., Nicolai-Shaw, N., Parinussa, R., Pratola, C., Reimer, C., van der Schalie, R., Seneviratne, S. I., Smolander, T., and Lecomte, P.: ESA CCI Soil Mois-

670 ture for improved Earth system understanding: State-of-the art and future directions, Remote Sensing of Environment, 203, 185–215, https://doi.org/https://doi.org/10.1016/j.rse.2017.07.001, earth Observation of Essential Climate Variables, 2017.

Dowd, E., Wilson, C., Chipperfield, M. P., Gloor, E., Manning, A., and Doherty, R.: Decreasing seasonal cycle amplitude of methane in the northern high latitudes being driven by lower-latitude changes in emissions and transport, Atmospheric Chemistry and Physics, 23, 7363–7382, https://doi.org/10.5194/acp-23-7363-2023, 2023.

675 East, J. D., Jacob, D. J., Balasus, N., Bloom, A. A., Bruhwiler, L., Chen, Z., Kaplan, J. O., Mickley, L. J., Mooring, T. A., Penn, E., Poulter, B., Sulprizio, M. P., Worden, J. R., Yantosca, R. M., and Zhang, Z.: Interpreting the Seasonality of Atmospheric Methane, Geophysical Research Letters, 51, e2024GL108 494, https://doi.org/10.1029/2024GL108494, e2024GL108494, 2024.

ECMWF: IFS Documentation CY45R1 - Part IV : Physical processes, 4, ECMWF, https://doi.org/10.21957/4whwo8jw0, 2018.

Erkkilä, A., Tenkanen, M., Tsuruta, A., Rautiainen, K., and Aalto, T.: Environmental and Seasonal Variability of High Lat-
680   itude Methane Emissions Based on Earth Observation Data and Atmospheric Inverse Modelling, Remote Sensing, 15,
         https://doi.org/10.3390/rs15245719, 2023.

ESA: SMOS Soil Freeze and Thaw State, Version 300, https://doi.org/doi.org/10.57780/sm1-fbf89e0, 2023.

Hachmeister, J., Schneising, O., Buchwitz, M., Lorente, A., Borsdorff, T., Burrows, J. P., Notholt, J., and Buschmann, M.: On the influence
         of underlying elevation data on Sentinel-5 Precursor TROPOMI satellite methane retrievals over Greenland, Atmospheric Measurement
685   Techniques, 15, 4063–4074, https://doi.org/10.5194/amt-15-4063-2022, 2022.

Hachmeister, J., Schneising, O., Buchwitz, M., Burrows, J. P., Notholt, J., and Buschmann, M.: Zonal variability of methane trends derived
         from satellite data, Atmospheric Chemistry and Physics, 24, 577–595, https://doi.org/10.5194/acp-24-577-2024, 2024.

Hersbach, H., Bell, B., Berrisford, P., Biavati, G., Horányi, A., Muñoz Sabater, J., Nicolas, J., Peubey, C., Radu, R., Rozum, I.,
         Schepers, D., Simmons, A., Soci, C., Dee, D., and Thépaut, J.-N.: ERA5 hourly data on single levels from 1940 to present,
690   https://doi.org/10.24381/cds.adbb2d47, accessed: 2024-03-07 and 2024-08-07, 2018.

Hersbach, H., Bell, B., Berrisford, P., Hirahara, S., Horányi, A., Muñoz-Sabater, J., Nicolas, J., Peubey, C., Radu, R., Schepers, D., Sim-
         mons, A., Soci, C., Abdalla, S., Abellan, X., Balsamo, G., Bechtold, P., Biavati, G., Bidlot, J., Bonavita, M., De Chiara, G., Dahlgren,
         P., Dee, D., Diamantakis, M., Dragani, R., Flemming, J., Forbes, R., Fuentes, M., Geer, A., Haimberger, L., Healy, S., Hogan, R. J.,
         Hólm, E., Janisková, M., Keeley, S., Laloyaux, P., Lopez, P., Lupu, C., Radnoti, G., de Rosnay, P., Rozum, I., Vamborg, F., Vil-
695   laume, S., and Thépaut, J.-N.: The ERA5 global reanalysis, Quarterly Journal of the Royal Meteorological Society, 146, 1999–2049,
         https://doi.org/https://doi.org/10.1002/qj.3803, 2020.

Houweling, S., Krol, M., Bergamaschi, P., Frankenberg, C., Dlugokencky, E. J., Morino, I., Notholt, J., Sherlock, V., Wunch, D., Beck, V.,
         Gerbig, C., Chen, H., Kort, E. A., Röckmann, T., and Aben, I.: A multi-year methane inversion using SCIAMACHY, accounting for
         systematic errors using TCCON measurements, Atmos. Chem. Phys., 14, 3991–4012, https://doi.org/10.5194/acp-14-3991-2014, 2014.

700 Howard, D., Agnan, Y., Helmig, D., Yang, Y., and Obrist, D.: Environmental controls on ecosystem-scale cold-season methane and carbon
         dioxide fluxes in an Arctic tundra ecosystem, Biogeosciences, 17, 4025–4042, https://doi.org/10.5194/bg-17-4025-2020, 2020.

Hu, H., Landgraf, J., Detmers, R., Borsdorff, T., Aan de Brugh, J., Aben, I., Butz, A., and Hasekamp, O.: Toward Global Mapping
         of Methane With TROPOMI: First Results and Intersatellite Comparison to GOSAT, Geophysical Research Letters, 45, 3682–3689,
         https://doi.org/https://doi.org/10.1002/2018GL077259, 2018.

705 Huijnen, V., Williams, J., van Weele, M., van Noije, T., Krol, M., Dentener, F., Segers, A., Houweling, S., Peters, W., de Laat, J., Boersma,
         F., Bergamaschi, P., van Velthoven, P., Le Sager, P., Eskes, H., Alkemade, F., Scheele, R., Nédélec, P., and Pätz, H.-W.: The global
         chemistry transport model TM5: description and evaluation of the tropospheric chemistry version 3.0, Geoscientific Model Development,
         3, 445–473, https://doi.org/10.5194/gmd-3-445-2010, publisher: Copernicus GmbH, 2010.

Jackson, R. B., Saunois, M., Martinez, A., Canadell, J. G., Yu, X., Li, M., Poulter, B., Raymond, P. A., Regnier, P., Ciais, P., Davis,
710   S. J., and Patra, P. K.: Human activities now fuel two-thirds of global methane emissions, Environmental Research Letters, 19, 101 002,
         https://doi.org/10.1088/1748-9326/ad6463, 2024.

Kittler, F., Heimann, M., Kolle, O., Zimov, N., Zimov, S., and Göckede, M.: Long-Term Drainage Reduces CO2 Uptake and CH4 Emissions in
         a Siberian Permafrost Ecosystem, Global Biogeochemical Cycles, 31, 1704–1717, https://doi.org/https://doi.org/10.1002/2017GB005774,
         2017.

715 Kivimäki, E., Lindqvist, H., Hakkarainen, J., Laine, M., Sussmann, R., Tsuruta, A., Detmers, R., Deutscher, N. M., Dlugokencky, E. J.,
         Hase, F., Hasekamp, O., Kivi, R., Morino, I., Notholt, J., Pollard, D. F., Roehl, C., Schneider, M., Sha, M. K., Velazco, V. A., Warneke,

T., Wunch, D., Yoshida, Y., and Tamminen, J.: Evaluation and Analysis of the Seasonal Cycle and Variability of the Trend from GOSAT Methane Retrievals, Remote Sensing, 11, https://doi.org/10.3390/rs11070882, 2019.

Krol, M., Houweling, S., Bregman, B., Broek, M. v. d., Segers, A., Velthoven, P. v., Peters, W., Dentener, F., and Bergamaschi, P.: The two-720 way nested global chemistry-transport zoom model TM5: algorithm and applications, Atmospheric Chemistry and Physics, 5, 417–432, https://doi.org/https://doi.org/10.5194/acp-5-417-2005, 2005.

Kuze, A., Suto, H., Nakajima, M., and Hamazaki, T.: Thermal and near infrared sensor for carbon observation Fourier-transform spectrometer on the Greenhouse Gases Observing Satellite for greenhouse gases monitoring, Appl. Opt., 48, 6716–6733, https://doi.org/10.1364/AO.48.006716, 2009.

725 Lelieveld, J., Gromov, S., Pozzer, A., and Taraborrelli, D.: Global tropospheric hydroxyl distribution, budget and reactivity, Atmospheric Chemistry and Physics, 16, 12 477–12 493, https://doi.org/10.5194/acp-16-12477-2016, 2016.

Liang, R., Zhang, Y., Chen, W., Zhang, P., Liu, J., Chen, C., Mao, H., Shen, G., Qu, Z., Chen, Z., Zhou, M., Wang, P., Parker, R. J., Boesch, H., Lorente, A., Maasakkers, J. D., and Aben, I.: East Asian methane emissions inferred from high-resolution inversions of GOSAT and TROPOMI observations: a comparative and evaluative analysis, Atmospheric Chemistry and Physics, 23, 8039–8057, 730 https://doi.org/10.5194/acp-23-8039-2023, 2023.

Lindqvist, H., Kivimäki, E., Häkkilä, T., Tsuruta, A., Schneising, O., Buchwitz, M., Lorente, A., Martinez Velarte, M., Borsdorff, T., Alberti, C., Backman, L., Buschmann, M., Chen, H., Dubravica, D., Hase, F., Heikkinen, P., Karppinen, T., Kivi, R., McGee, E., Notholt, J., Rautiainen, K., Roche, S., Simpson, W., Strong, K., Tu, Q., Wunch, D., Aalto, T., and Tamminen, J.: Evaluation of Sentinel-5P TROPOMI Methane Observations at Northern High Latitudes, Remote Sensing, 16, https://doi.org/10.3390/rs16162979, 2024.

735 Lorente, A., Borsdorff, T., Butz, A., Hasekamp, O., aan de Brugh, J., Schneider, A., Wu, L., Hase, F., Kivi, R., Wunch, D., Pollard, D. F., Shiomi, K., Deutscher, N. M., Velazco, V. A., Roehl, C. M., Wennberg, P. O., Warneke, T., and Landgraf, J.: Methane retrieved from TROPOMI: improvement of the data product and validation of the first 2 years of measurements, Atmospheric Measurement Techniques, 14, 665–684, https://doi.org/10.5194/amt-14-665-2021, 2021.

Lorente, A., Borsdorff, T., Martinez-Velarte, M. C., Butz, A., Hasekamp, O. P., Wu, L., and Landgraf, J.: Evaluation of the methane 740 full-physics retrieval applied to TROPOMI ocean sun glint measurements, Atmospheric Measurement Techniques, 15, 6585–6603, https://doi.org/10.5194/amt-15-6585-2022, 2022.

Luojus, K., Pulliainen, J., Takala, M., Lemmetyinen, J., Mortimer, C., Derksen, C., Mudryk, L., Moisander, M., Hiltunen, M., Smolander, T., Ikonen, J., Cohen, J., Salminen, M., Norberg, J., Veijola, K., and Venäläinen, P.: GlobSnow v3.0 Northern Hemisphere snow water equivalent dataset, Scientific Data, 8, 163, https://doi.org/10.1038/s41597-021-00939-2, 2021.

745 Mastepanov, M., Sigsgaard, C., Tagesson, T., Ström, L., Tamstorf, M. P., Lund, M., and Christensen, T. R.: Revisiting factors controlling methane emissions from high-Arctic tundra, Biogeosciences, 10, 5139–5158, https://doi.org/10.5194/bg-10-5139-2013, 2013.

Mikkonen, A., Lindqvist, H., Peltoniemi, J., and Tamminen, J.: Non-Lambertian snow surface reflection models for simulated top-of-the-atmosphere radiances in the NIR and SWIR wavelengths, Journal of Quantitative Spectroscopy and Radiative Transfer, 315, 108 892, https://doi.org/https://doi.org/10.1016/j.jqsrt.2023.108892, 2024.

750 Muñoz Sabater, J., Dutra, E., Agustí-Panareda, A., Albergel, C., Arduini, G., Balsamo, G., Boussetta, S., Choulga, M., Harrigan, S., Hersbach, H., Martens, B., Miralles, D. G., Piles, M., Rodríguez-Fernández, N. J., Zsoter, E., Buontempo, C., and Thépaut, J.-N.: ERA5-Land: a state-of-the-art global reanalysis dataset for land applications, Earth System Science Data, 13, 4349–4383, https://doi.org/10.5194/essd-13-4349-2021, 2021.

NOAA, Earth System Research Laboratories, G. M. L.: Curve Fitting Methods Applied to Time Series in NOAA/ESRL/GMD, https://gml.
755   noaa.gov/ccgg/mbl/crvfit/crvfit.html, accessed: 2024-04-10, 2012.

Olefeldt, D., Hovemyr, M., Kuhn, M. A., Bastviken, D., Bohn, T. J., Connolly, J., Crill, P., Euskirchen, E. S., Finkelstein, S. A., Genet,
    H., Grosse, G., Harris, L. I., Heffernan, L., Helbig, M., Hugelius, G., Hutchins, R., Juutinen, S., Lara, M. J., Malhotra, A., Manies, K.,
    McGuire, A. D., Natali, S. M., O'Donnell, J. A., Parmentier, F.-J. W., Räsänen, A., Schädel, C., Sonnentag, O., Strack, M., Tank, S. E.,
    Treat, C., Varner, R. K., Virtanen, T., Warren, R. K., and Watts, J. D.: The Boreal–Arctic Wetland and Lake Dataset (BAWLD), Earth
760   System Science Data, 13, 5127–5149, https://doi.org/10.5194/essd-13-5127-2021, 2021.

Oliva, R., Daganzo, E., Richaume, P., Kerr, Y., Cabot, F., Soldo, Y., Anterrieu, E., Reul, N., Gutierrez, A., Barbosa, J., and Lopes, G.: Status
    of Radio Frequency Interference (RFI) in the 1400-1427 MHz passive band based on six years of SMOS mission, Remote Sensing of
    Environment, 180, 64–75, https://doi.org/10.1016/j.rse.2016.01.013, 2016.

Pandey, S., Houweling, S., Krol, M., Aben, I., Chevallier, F., Dlugokencky, E. J., Gatti, L. V., Gloor, E., Miller, J. B., Detmers, R., Machida,
765   T., and Röckmann, T.: Inverse modeling of GOSAT-retrieved ratios of total column CH_4 and CO_2 for 2009 and 2010, Atmospheric
    Chemistry and Physics, 16, 5043–5062, https://doi.org/10.5194/acp-16-5043-2016, 2016.

Parker, R. J., Boesch, H., McNorton, J., Comyn-Platt, E., Gloor, M., Wilson, C., Chipperfield, M. P., Hayman, G. D., and Bloom, A. A.: Eval-
    uating year-to-year anomalies in tropical wetland methane emissions using satellite CH4 observations, Remote Sensing of Environment,
    211, 261–275, https://doi.org/https://doi.org/10.1016/j.rse.2018.02.011, 2018.

770   Pedregosa, F., Varoquaux, G., Gramfort, A., Michel, V., Thirion, B., Grisel, O., Blondel, M., Prettenhofer, P., Weiss, R., Dubourg, V.,
    Vanderplas, J., Passos, A., Cournapeau, D., Brucher, M., Perrot, M., and Duchesnay, E.: Scikit-learn: Machine Learning in Python, J.
    Mach. Learn. Res., 12, 2825–2830, 2011.

Pickers, P. A. and Manning, A. C.: Investigating bias in the application of curve fitting programs to atmospheric time series, Atmospheric
    Measurement Techniques, 8, 1469–1489, https://doi.org/10.5194/amt-8-1469-2015, 2015.

775   Prinn, R. G., Huang, J., Weiss, R. F., Cunnold, D. M., Fraser, P. J., Simmonds, P. G., McCulloch, A., Harth, C., Salameh, P., O'Doherty,
    S., Wang, R. H. J., Porter, L., and Miller, B. R.: Evidence for Substantial Variations of Atmospheric Hydroxyl Radicals in the Past Two
    Decades, Science, 292, 1882–1888, https://doi.org/10.1126/science.1058673, 2001.

Rantanen, M., Karpechko, A. Y., Lipponen, A., Nordling, K., Hyvärinen, O., Ruosteenoja, K., Vihma, T., and Laaksonen, A.: The Arctic has
    warmed nearly four times faster than the globe since 1979, Communications Earth & Environment, 3, 168, https://doi.org/10.1038/s43247-
780   022-00498-3, 2022.

Rautiainen, K., Parkkinen, T., Lemmetyinen, J., Schwank, M., Wiesmann, A., Ikonen, J., Derksen, C., Davydov, S., Davydova, A., Boike, J.,
    Langer, M., Drusch, M., and Pulliainen, J.: SMOS prototype algorithm for detecting autumn soil freezing, Remote Sensing of Environment,
    180, 346–360, https://doi.org/https://doi.org/10.1016/j.rse.2016.01.012, special Issue: ESA's Soil Moisture and Ocean Salinity Mission -
    Achievements and Applications, 2016.

785   Rehder, Z., Kleinen, T., Kutzbach, L., Stepanenko, V., Langer, M., and Brovkin, V.: Simulated methane emissions from Arctic ponds are
    highly sensitive to warming, Biogeosciences, 20, 2837–2855, https://doi.org/10.5194/bg-20-2837-2023, 2023.

Rinne, J., Riutta, T., Pihlatie, M., Aurela, M., Haapanala, S., and Tuovinen, J.-P.: Annual cycle of methane emission from a boreal fen
    measured by the eddy covariance technique, Tellus B: Chemical and Physical Meteorology, 59, 449–457, https://doi.org/10.1111/j.1600-
    0889.2007.00261.x, 2007.

790   Rinne, J., Tuittila, E.-S., Peltola, O., Li, X., Raivonen, M., Alekseychik, P., Haapanala, S., Pihlatie, M., Aurela, M., Mammarella, I., and
        Vesala, T.: Temporal Variation of Ecosystem Scale Methane Emission From a Boreal Fen in Relation to Temperature, Water Table Position,
        and Carbon Dioxide Fluxes, Global Biogeochemical Cycles, 32, 1087–1106, https://doi.org/https://doi.org/10.1029/2017GB005747, 2018.

      Rößger, N., Sachs, T., Wille, C., Boike, J., and Kutzbach, L.: Seasonal increase of methane emissions linked to warming in Siberian tundra,
        Nature Climate Change, 12, 1031–1036, https://doi.org/10.1038/s41558-022-01512-4, 2022.

795   Saunois, M., Stavert, A. R., Poulter, B., Bousquet, P., Canadell, J. G., Jackson, R. B., Raymond, P. A., Dlugokencky, E. J., Houweling, S.,
        Patra, P. K., Ciais, P., Arora, V. K., Bastviken, D., Bergamaschi, P., Blake, D. R., Brailsford, G., Bruhwiler, L., Carlson, K. M., Carrol,
        M., Castaldi, S., Chandra, N., Crevoisier, C., Crill, P. M., Covey, K., Curry, C. L., Etiope, G., Frankenberg, C., Gedney, N., Hegglin,
        M. I., Höglund-Isaksson, L., Hugelius, G., Ishizawa, M., Ito, A., Janssens-Maenhout, G., Jensen, K. M., Joos, F., Kleinen, T., Krummel,
        P. B., Langenfelds, R. L., Laruelle, G. G., Liu, L., Machida, T., Maksyutov, S., McDonald, K. C., McNorton, J., Miller, P. A., Melton,
800   J. R., Morino, I., Müller, J., Murguia-Flores, F., Naik, V., Niwa, Y., Noce, S., O'Doherty, S., Parker, R. J., Peng, C., Peng, S., Peters, G. P.,
        Prigent, C., Prinn, R., Ramonet, M., Regnier, P., Riley, W. J., Rosentreter, J. A., Segers, A., Simpson, I. J., Shi, H., Smith, S. J., Steele, L. P.,
        Thornton, B. F., Tian, H., Tohjima, Y., Tubiello, F. N., Tsuruta, A., Viovy, N., Voulgarakis, A., Weber, T. S., van Weele, M., van der Werf,
        G. R., Weiss, R. F., Worthy, D., Wunch, D., Yin, Y., Yoshida, Y., Zhang, W., Zhang, Z., Zhao, Y., Zheng, B., Zhu, Q., Zhu, Q., and Zhuang,
        Q.: The Global Methane Budget 2000–2017, Earth System Science Data, 12, 1561–1623, https://doi.org/10.5194/essd-12-1561-2020,
805   2020.

      Saunois, M., Martinez, A., Poulter, B., Zhang, Z., Raymond, P., Regnier, P., Canadell, J. G., Jackson, R. B., Patra, P. K., Bousquet, P., Ciais,
        P., Dlugokencky, E. J., Lan, X., Allen, G. H., Bastviken, D., Beerling, D. J., Belikov, D. A., Blake, D. R., Castaldi, S., Crippa, M., Deemer,
        B. R., Dennison, F., Etiope, G., Gedney, N., Höglund-Isaksson, L., Holgerson, M. A., Hopcroft, P. O., Hugelius, G., Ito, A., Jain, A. K.,
        Janardanan, R., Johnson, M. S., Kleinen, T., Krummel, P., Lauerwald, R., Li, T., Liu, X., McDonald, K. C., Melton, J. R., Mühle, J.,
810   Müller, J., Murguia-Flores, F., Niwa, Y., Noce, S., Pan, S., Parker, R. J., Peng, C., Ramonet, M., Riley, W. J., Rocher-Ros, G., Rosentreter,
        J. A., Sasakawa, M., Segers, A., Smith, S. J., Stanley, E. H., Thanwerdas, J., Tian, H., Tsuruta, A., Tubiello, F. N., Weber, T. S., van der
        Werf, G., Worthy, D. E., Xi, Y., Yoshida, Y., Zhang, W., Zheng, B., Zhu, Q., Zhu, Q., and Zhuang, Q.: Global Methane Budget 2000–2020,
        Earth System Science Data Discussions, 2024, 1–147, https://doi.org/10.5194/essd-2024-115, 2024.

      Schneising, O., Buchwitz, M., Reuter, M., Bovensmann, H., Burrows, J. P., Borsdorff, T., Deutscher, N. M., Feist, D. G., Griffith, D. W. T.,
815   Hase, F., Hermans, C., Iraci, L. T., Kivi, R., Landgraf, J., Morino, I., Notholt, J., Petri, C., Pollard, D. F., Roche, S., Shiomi, K., Strong, K.,
        Sussmann, R., Velazco, V. A., Warneke, T., and Wunch, D.: A scientific algorithm to simultaneously retrieve carbon monoxide and methane
        from TROPOMI onboard Sentinel-5 Precursor, Atmospheric Measurement Techniques, 12, 6771–6802, https://doi.org/10.5194/amt-12-
        6771-2019, 2019.

      Schneising, O., Buchwitz, M., Hachmeister, J., Vanselow, S., Reuter, M., Buschmann, M., Bovensmann, H., and Burrows, J. P.: Advances
820   in retrieving XCH$_4$ and XCO from Sentinel-5 Precursor: improvements in the scientific TROPOMI/WFMD algorithm, Atmospheric
        Measurement Techniques, 16, 669–694, https://doi.org/10.5194/amt-16-669-2023, 2023.

      Skeie, R. B., Øivind Hodnebrog, and Myhre, G.: Trends in atmospheric methane concentrations since 1990 were driven and modified by
        anthropogenic emissions, Communications Earth & Environment, 4, 317, https://doi.org/10.1038/s43247-023-00969-1, 2023.

      Spivakovsky, C. M., Logan, J. A., Montzka, S. A., Balkanski, Y. J., Foreman-Fowler, M., Jones, D. B. A., Horowitz, L. W., Fusco, A. C.,
825   Brenninkmeijer, C. a. M., Prather, M. J., Wofsy, S. C., and McElroy, M. B.: Three-dimensional climatological distribution of tropospheric
        OH: Update and evaluation, Journal of Geophysical Research: Atmospheres, 105, 8931–8980, https://doi.org/10.1029/1999JD901006,
        2000.

Takala, M., Luojus, K., Pulliainen, J., Derksen, C., Lemmetyinen, J., Kärnä, J.-P., Koskinen, J., and Bojkov, B.: Estimating northern hemisphere snow water equivalent for climate research through assimilation of space-borne radiometer data and ground-based measurements,
830   Remote Sensing of Environment, 115, 3517–3529, https://doi.org/https://doi.org/10.1016/j.rse.2011.08.014, 2011.

Tenkanen, M., Tsuruta, A., Rautiainen, K., Kangasaho, V., Ellul, R., and Aalto, T.: Utilizing Earth Observations of Soil Freeze/Thaw Data and Atmospheric Concentrations to Estimate Cold Season Methane Emissions in the Northern High Latitudes, Remote Sensing, 13, https://doi.org/10.3390/rs13245059, 2021.

Thoning, K. W., Tans, P. P., and Komhyr, W. D.: Atmospheric carbon dioxide at Mauna Loa Observatory: 2. Anal-
835   ysis of the NOAA GMCC data, 1974–1985, Journal of Geophysical Research: Atmospheres, 94, 8549–8565, https://doi.org/https://doi.org/10.1029/JD094iD06p08549, 1989.

Travis, K. R., Heald, C. L., Allen, H. M., Apel, E. C., Arnold, S. R., Blake, D. R., Brune, W. H., Chen, X., Commane, R., Crounse, J. D., Daube, B. C., Diskin, G. S., Elkins, J. W., Evans, M. J., Hall, S. R., Hintsa, E. J., Hornbrook, R. S., Kasibhatla, P. S., Kim, M. J., Luo, G., McKain, K., Millet, D. B., Moore, F. L., Peischl, J., Ryerson, T. B., Sherwen, T., Thames, A. B., Ullmann, K., Wang, X., Wennberg,
840   P. O., Wolfe, G. M., and Yu, F.: Constraining remote oxidation capacity with ATom observations, Atmos. Chem. Phys., 20, 7753–7781, https://doi.org/10.5194/acp-20-7753-2020, 2020.

Tsuruta, A., Aalto, T., Backman, L., Hakkarainen, J., Laan-Luijkx, I. T. v. d., Krol, M. C., Spahni, R., Houweling, S., Laine, M., Dlugokencky, E., Gomez-Pelaez, A. J., Schoot, M. v. d., Langenfelds, R., Ellul, R., Arduini, J., Apadula, F., Gerbig, C., Feist, D. G., Kivi, R., Yoshida, Y., and Peters, W.: Global methane emission estimates for 2000–2012 from CarbonTracker Europe-CH$_4$ v1.0, Geoscientific
845   Model Development, 10, 1261–1289, https://doi.org/doi:10.5194/gmd-10-1261-2017, 2017.

Tsuruta, A., Kivimäki, E., Lindqvist, H., Karppinen, T., Backman, L., Hakkarainen, J., Schneising, O., Buchwitz, M., Lan, X., Kivi, R., Chen, H., Buschmann, M., Herkommer, B., Notholt, J., Roehl, C., Té, Y., Wunch, D., Tamminen, J., and Aalto, T.: CH4 Fluxes Derived from Assimilation of TROPOMI XCH4 in CarbonTracker Europe-CH4: Evaluation of Seasonality and Spatial Distribution in the Northern High Latitudes, Remote Sensing, 15, https://doi.org/10.3390/rs15061620, 2023.

850   Turner, A. J., Frankenberg, C., Wennberg, P. O., and Jacob, D. J.: Ambiguity in the causes for decadal trends in atmospheric methane and hydroxyl, Proceedings of the National Academy of Sciences, 114, 5367–5372, https://doi.org/10.1073/pnas.1616020114, 2017.

U.S. National Ice Center.: IMS Daily Northern Hemisphere Snow and Ice Analysis at 1 km, 4 km, and 24 km Resolutions, Version 1 (24km subset), https://doi.org/10.7265/N52R3PMC, updated daily, 2008.

Vanselow, S., Schneising, O., Buchwitz, M., Reuter, M., Bovensmann, H., Boesch, H., and Burrows, J. P.: Automated detection of regions
855   with persistently enhanced methane concentrations using Sentinel-5 Precursor satellite data, Atmospheric Chemistry and Physics, 24, 10 441–10 473, https://doi.org/10.5194/acp-24-10441-2024, 2024.

Virkkala, A.-M., Niittynen, P., Kemppinen, J., Marushchak, M. E., Voigt, C., Hensgens, G., Kerttula, J., Happonen, K., Tyystjärvi, V., Biasi, C., Hultman, J., Rinne, J., and Luoto, M.: High-resolution spatial patterns and drivers of terrestrial ecosystem carbon dioxide, methane, and nitrous oxide fluxes in the tundra, Biogeosciences, 21, 335–355, https://doi.org/10.5194/bg-21-335-2024, 2024.

860   Wolfe, G. M., Nicely, J. M., Clair, J. M. S., Hanisco, T. F., Liao, J., Oman, L. D., Brune, W. B., Miller, D., Thames, A., Abad, G. G., Ryerson, T. B., Thompson, C. R., Peischl, J., McKain, K., Sweeney, C., Wennberg, P. O., Kim, M., Crounse, J. D., Hall, S. R., Ullmann, K., Diskin, G., Bui, P., Chang, C., and Dean-Day, J.: Mapping hydroxyl variability throughout the global remote troposphere via synthesis of airborne and satellite formaldehyde observations, Proceedings of the National Academy of Sciences, 116, 11 171–11 180, https://doi.org/10.1073/pnas.1821661116, 2019.

865   Zhang, Y., Jacob, D. J., Maasakkers, J. D., Sulprizio, M. P., Sheng, J.-X., Gautam, R., and Worden, J.: Monitoring global tropospheric OH concentrations using satellite observations of atmospheric methane, Atmospheric Chemistry and Physics, 18, 15 959–15 973, https://doi.org/10.5194/acp-18-15959-2018, 2018.

Zhao, Y., Saunois, M., Bousquet, P., Lin, X., Berchet, A., Hegglin, M. I., Canadell, J. G., Jackson, R. B., Hauglustaine, D. A., Szopa, S., Stavert, A. R., Abraham, N. L., Archibald, A. T., Bekki, S., Deushi, M., Jöckel, P., Josse, B., Kinnison, D., Kirner, O., Marécal, V.,

870   O'Connor, F. M., Plummer, D. A., Revell, L. E., Rozanov, E., Stenke, A., Strode, S., Tilmes, S., Dlugokencky, E. J., and Zheng, B.: Inter-model comparison of global hydroxyl radical (OH) distributions and their impact on atmospheric methane over the 2000–2016 period, Atmospheric Chemistry and Physics, 19, 13 701–13 723, https://doi.org/10.5194/acp-19-13701-2019, 2019.

Zona, D., Gioli, B., Commane, R., Lindaas, J., Wofsy, S. C., Miller, C. E., Dinardo, S. J., Dengel, S., Sweeney, C., Karion, A., Chang, R. Y. W., Henderson, J. M., Murphy, P. C., Goodrich, J. P., Moreaux, V., Liljedahl, A., Watts, J. D., Kimball, J. S., Lipson, D. A., and

875   Oechel, W. C.: Cold season emissions dominate the Arctic tundra methane budget, PROCEEDINGS OF THE NATIONAL ACADEMY OF SCIENCES OF THE UNITED STATES OF AMERICA, 113, 40–45, https://doi.org/10.1073/pnas.1516017113, 2015.